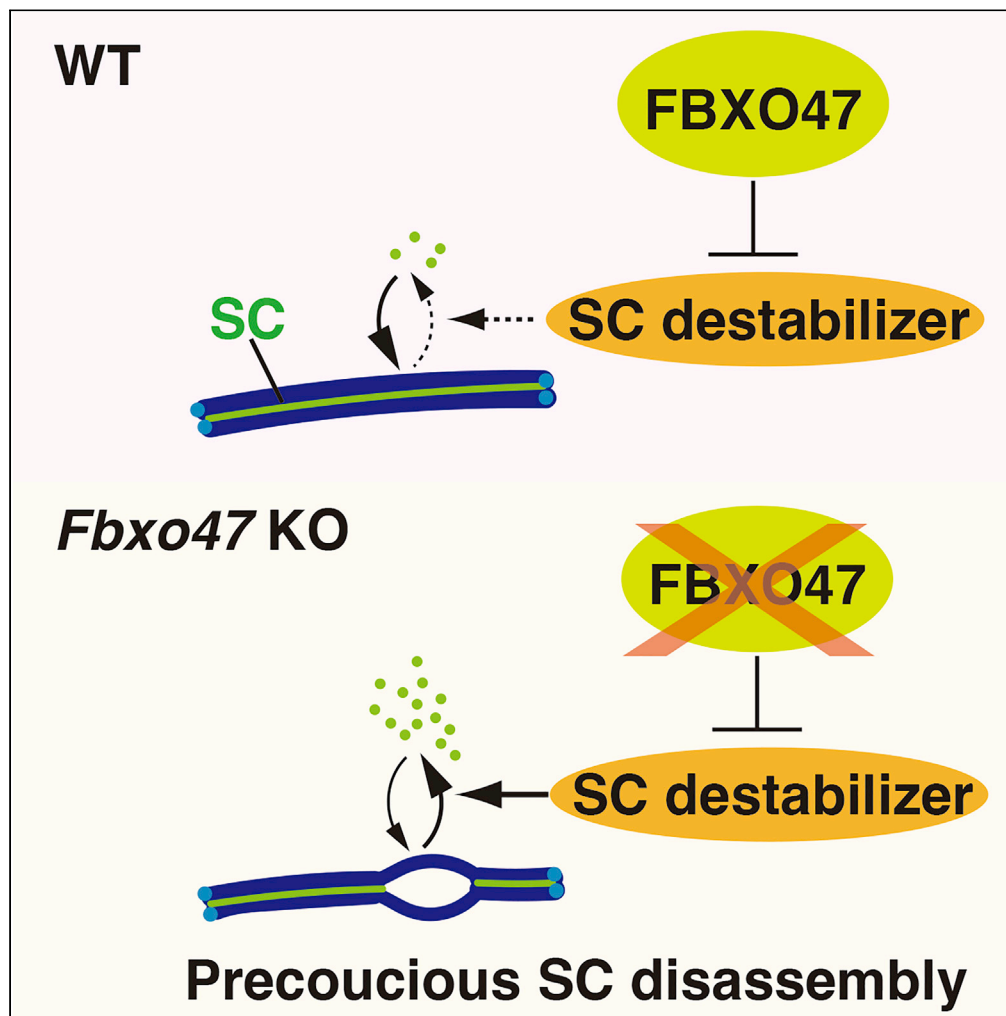# iScience

Article

FBXO47 is essential for preventing the synaptonemal complex from premature disassembly in mouse male meiosis

Nobuhiro Tanno, Kazumasa Takemoto, Yuki Takada-Horisawa, ..., Naoki Takeda, Kimi Araki, Kei-ichiro Ishiguro

ishiguro@kumamoto-u.ac.jp

Highlights

FBXO47 is a stabilizer of the synaptonemal complex during male meiotic prophase

FBXO47 KO shows precocious disassembly of the synaptonemal complex

FBXO47 may function independently of SCF E3 ligase to maintain homolog synapsis

Article

FBXO47 is essential for preventing the synaptonemal complex from premature disassembly in mouse male meiosis

Nobuhiro Tanno,[1,4] Kazumasa Takemoto,[1,4] Yuki Takada-Horisawa,[1] Ryuki Shimada,[1] Sayoko Fujimura,[2] Naoki Tani,[2] Naoki Takeda,[3] Kimi Araki,[3] and Kei-ichiro Ishiguro[1,5,*]

SUMMARY

Meiotic prophase I is a prolonged G2 phase that ensures the completion of numerous meiosis-specific chromosome events. During meiotic prophase I, homologous chromosomes undergo synapsis to facilitate meiotic recombination yielding crossovers. It remains largely elusive how homolog synapsis is temporally maintained and destabilized during meiotic prophase I. Here we show that FBXO47 is the stabilizer of the synaptonemal complex during male meiotic prophase I. Disruption of FBXO47 shows severe impact on homologous chromosome synapsis, meiotic recombination, and XY body formation, leading to male infertility. Notably, in the absence of FBXO47, although once homologous chromosomes are synapsed, the synaptonemal complex is precociously disassembled before progressing beyond pachytene. Remarkably, *Fbxo47* KO spermatocytes remain in an earlier stage of meiotic prophase I and lack crossovers, despite apparently exhibiting diplotene-like chromosome morphology. We propose that FBXO47 plays a crucial role in preventing the synaptonemal complex from premature disassembly during cell cycle progression of meiotic prophase I.

INTRODUCTION

Meiosis consists of a single DNA replication followed by two rounds of chromosome segregation, which halves the chromosome number to ultimately produce haploid gametes. During meiotic prophase I, sister chromatids are organized into proteinaceous structures, termed axial element (AE) or chromosome axis (Zickler and Kleckner, 2015). Homologous chromosomes (homologs) then undergo synapsis, which is promoted by the assembly of synaptonemal complex (SC) (Cahoon and Hawley, 2016). Homolog synapsis facilitates meiotic recombination yielding crossovers, a process that produces physical linkages called chiasmata between the homologs (Baudat et al., 2013; Keeney et al., 2014). Although homolog synapsis persists until meiotic recombination is completed during pachytene, it is dissolved upon diplotene-Metaphase I transition. Thus, homolog synapsis and desynapsis are temporally regulated. However, it remains elusive how homolog synapsis is temporally maintained and destabilized during meiotic prophase I.

SCF (SKP1–Cullin–F-box) E3 ubiquitin ligase is a key regulator of cell cycle (Cardozo and Pagano, 2004; Deshaies, 1999). Accumulating lines of evidence suggest that SCF is involved in homolog synapsis in a wide variety of organisms. In mouse, homologous chromosomes showed premature desynapsis in *Skp1* conditional KO spermatocytes (Guan et al., 2020), suggesting that SCF is required for the maintenance of SC during male meiotic prophase I. In *Drosophila* female, SkpA, a SKP1 homolog, is required for the assembly and/or the maintenance of SC (Barbosa et al., 2021). In budding yeast *Saccharomyces cerevisiae*, depletion of *Cdc53* that encodes Cullin resulted in defects in SC formation (Zhu et al., 2021). Thus, SCF is involved in the process of homolog synapsis during meiotic prophase I in diverse organisms.

Fbox-domain containing proteins act as a substrate recognition subunit in SCF E3 ubiquitin ligase (Jin et al., 2004; Kipreos and Pagano, 2000; Reitsma et al., 2017). It has been shown that Fbox-domain containing proteins are involved in homolog synapsis in a wide variety of organisms. In rice plant, *Oryza sativa*, mutants of MEIOTIC F-box *MOF* (He et al., 2016) and another Fbox *ZYG O 1* (Zhang et al., 2017) showed defects in DNA double-strand break (DSB) repair and bouquet formation during meiotic prophase I. In budding yeast, temperature-sensitive mutant of *Cdc4* that encodes F-box protein showed defective SC

[1]Department of Chromosome Biology, Institute of Molecular Embryology and Genetics (IMEG), Kumamoto University, Kumamoto 860-0811, Japan

[2]Liaison Laboratory Research Promotion Center, IMEG, Kumamoto University, Kumamoto 860-0811, Japan

[3]Institute of Resource Development and Analysis and Center for Metabolic Regulation of Healthy Aging, Kumamoto University, Kumamoto 860-0811, Japan

[4]These authors contributed equally

[5]Lead contact

*Correspondence: ishiguro@kumamoto-u.ac.jp
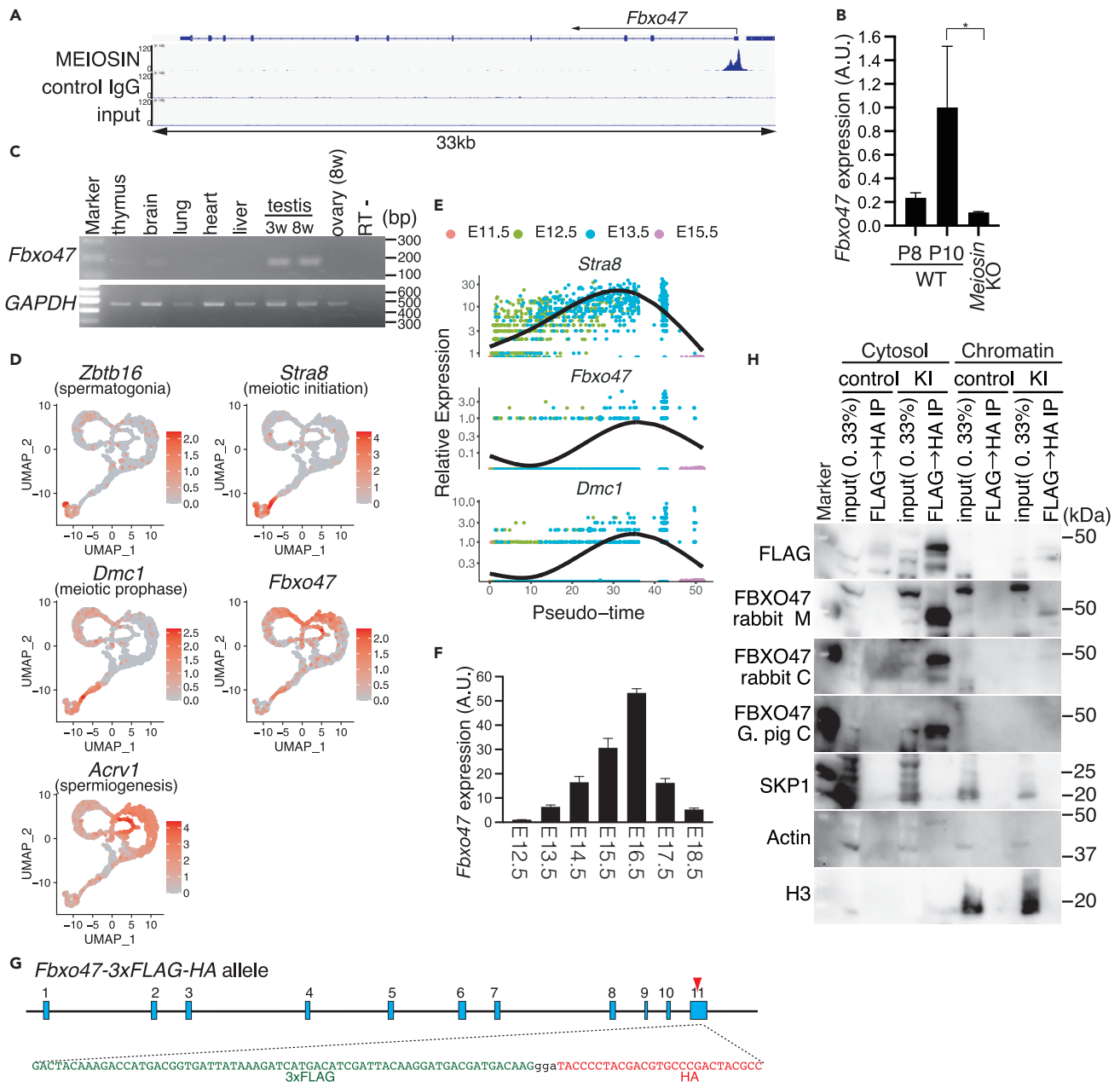https://doi.org/10.1016/j.isci.2022.104008

Figure 1. Identification of the meiosis-specific factor FBXO47

(A) Genomic view of MEIOSIN binding peak over *Fbxo47* loci. Genomic coordinates were obtained from Ensembl.

(B) The expression of *Fbxo47* in WT and *Meiosin* KO was examined using RT-PCR. Testis RNA was obtained from WT (3 animals each for P8 and P10) and *Meiosin* KO (3 animals, P10). The graph shows the expression level of *Fbxo47* normalized by that of *GAPDH*. Data are represented as mean with SD. Expression level of *Fbxo47* in P10 WT was set to 1. Statistical significance was determined by one-way ANOVA for all the dataset (p =0.0221). For pair-wise comparison between P10 WT and *Meiosin* KO, statistical significance is shown by p value (Two-tailed t-test). *: p < 0.05.

(C) The tissue-specific expression pattern of *Fbxo47* was examined by RT-PCR. Testis RNA was obtained from embryonic day 18 (E18), 3-weeks old (3w) and 8-weeks old (8w) male mice. Ovary RNA was obtained from adult 8-weeks old (8w) female mice. RT-indicates control PCR without reverse transcription.

(D) Expression patterns of *Fbxo47* and other key developmental genes are reanalyzed using public scRNA-seq data of spermatogenic cells in adult mouse testis (GEO: GSE109033). Expression patterns of *Fbxo47* and other key developmental genes are shown in UMAP plots. Key developmental genes include *Zbtb16*: spermatogonia, *Stra8*: differentiating spermatogonia and preleptotene spermatocyte, *Dmc1*: meiotic prophase I spermatocyte, *Acrv1*: round and elongated spermatid. UMAP of *Zbtb16 and Stra8* was adopted from our previous study.

(E) Expression profiles of *Fbxo47, Stra8,* and *Dmc1* in E11.5, E12.5, E13.5, and E15.5 fetal ovaries along pseudotime trajectory of germ cells. Pseudotime analysis was performed by reanalyzing scRNA-seq data (DRA011172). Pseudotime expression profile of *Stra8* was adopted from our previous study.

Figure 1. *Continued*

(F) The expression pattern of *Fbxo47* in the embryonic ovary was examined by RT-qPCR. Average values normalized to E12.5 gonads are shown from technical triplicates or quadruplicates. Data are represented as mean with SD N = 1 gonadal sample for each embryo.

(G) Schematic illustrations of the *Fbxo47-3xFLAG-HA* knock-in (*Fbxo47-3FH* KI) allele. Blue boxes represent exons. The stop codon in the exon 11 was replaced with in-frame *3xFLAG-HA* and the endogenous 3′UTR.

(H) Western blot showed immunoprecipitates after tandem affinity purifications using anti-FLAG and anti-HA from cytoplasmic and chromatin extracts of WT (untagged control) and *Fbxo47-3FH* KI mouse testes (P15-18). The same membrane was sequentially reblotted with different antibodies against the endogenous FBXO47 that we generated. rabbit M: rabbit anti-FBXO47 middle region, rabbit (C) rabbit anti-FBXO47 C-terminal region, (G) pig (C) guinea pig anti-FBXO47 C-terminal region.

formation and DSB repair (Zhu et al., 2021). In *Drosophila* female, depletion of Slmb (βTrcp) and CG6758 (Fbxo42) caused impaired assembly and/or premature disassembly of SC (Barbosa et al., 2021). Although the substrates are yet to be identified in most of the cases, Fbox-domain containing proteins directly or indirectly regulate the assembly and disassembly of SC.

Previously, we identified MEIOSIN that plays an essential role in meiotic initiation both in mouse male and female (Ishiguro et al., 2020). MEIOSIN together with STRA8 (Kojima et al., 2019) activates meiotic genes and directs the switching from mitosis to meiosis. In the present study, we identified the *Fbxo47* gene that encodes a Fbox protein, as one of the MEIOSIN/STRA8-target genes. Previous genetic studies suggested FBXO47 homologs are implicated in the progression of meiotic prophase I in different species. In *C. elegance,* mutation in *prom-1* that encodes putative *Fbxo47* homolog, showed reduced homologous chromosome pairing and bivalent formation (Jantsch et al., 2007). In medaka fish, *fbxo47* mutant fails to complete meiotic prophase I in females but switches developmental fate from oogenesis into spermatogenesis (Kikuchi et al., 2020). In mouse, the *Fbxo47* gene that has previously been identified as a meiotic gene by single cell RNA-seq analysis of testes is essential for mouse spermatogenesis (Chen et al., 2018). FBXO47 interacts with SKP1 *in vitro* and disruption of FBXO47 led to the failure in completing homolog synapsis (Hua et al., 2019). Although previous studies suggested that FBXO47 homologs and distant meiotic Fbox-domain containing proteins play a role in homologous chromosome pairing/synapsis and meiotic recombination in a wide variety of organisms, the precise mechanisms how these proteins are involved in these processes remained elusive. Furthermore, whether FBXO47 is indeed involved in the function of SCF is unknown.

Here we show that mouse FBXO47 is essential for maintaining homolog synapsis during meiotic prophase I. FBXO47 is a cytoplasmic protein rather than a telomere binding protein. We demonstrate that in *Fbxo47* KO spermatocytes, homologous chromosome synapsis is complete, but SC is precociously disassembled. Further, we show that *Fbxo47* KO spermatocytes fail to progress beyond pachytene and remain in earlier meiotic prophase I in terms of cell cycle progression, despite the apparent exhibition of diplotene-like morphology of chromosomes. We propose that FBXO47 is essential for preventing SC from premature destruction during cell cycle progression of male meiotic prophase I. Further, we discuss the different observations and interpretations between the present study and the previous study on FBXO47 (Hua et al., 2019).

RESULTS

FBXO47 is expressed in mouse testes

Previously, we demonstrated that MEIOSIN collaborating with STRA8 activates meiotic genes, which are required for numerous meiotic events (Ishiguro et al., 2020). In spermatocytes, we identified *Fbxo47* as one of the MEIOSIN/STRA8-bound genes (Figure 1A). Our previous RNA-seq analysis showed that expression of *Fbxo47* was significantly downregulated in *Meiosin* KO testes at postnatal day 10 (P10) when a cohort of spermatocytes should undergo the first wave of meiotic entry (Ishiguro et al., 2020). We confirmed this by RT-qPCR analysis demonstrating that *Fbxo47* expression level was indeed downregulated in *Meiosin* KO testis at P10 (Figure 1B). We further examined the expression patterns of *Fbxo47* in different mouse tissues by RT-PCR analysis. *Fbxo47* gene showed higher expression levels in adult testis compared to other adult organs that we examined (Figure 1C). Spermatogenic expression of *Fbxo47* gene was further confirmed by the reanalysis of previous scRNA-seq data of adult mouse testis (Hermann et al., 2018) (Figure 1D). The result indicated that *Fbxo47* was coordinately expressed with the landmark genes of meiotic spermatocyte such as *Dmc1*, and spermatid at spermiogenesis such as *Acrv1*, rather than those of spermatogonia such as *Zbtb16* (Figure 1D). We noticed that *Fbxo47* mRNA was expressed weakly in meiotic spermatocytes, and highly in spermatids in testes, which is consistent
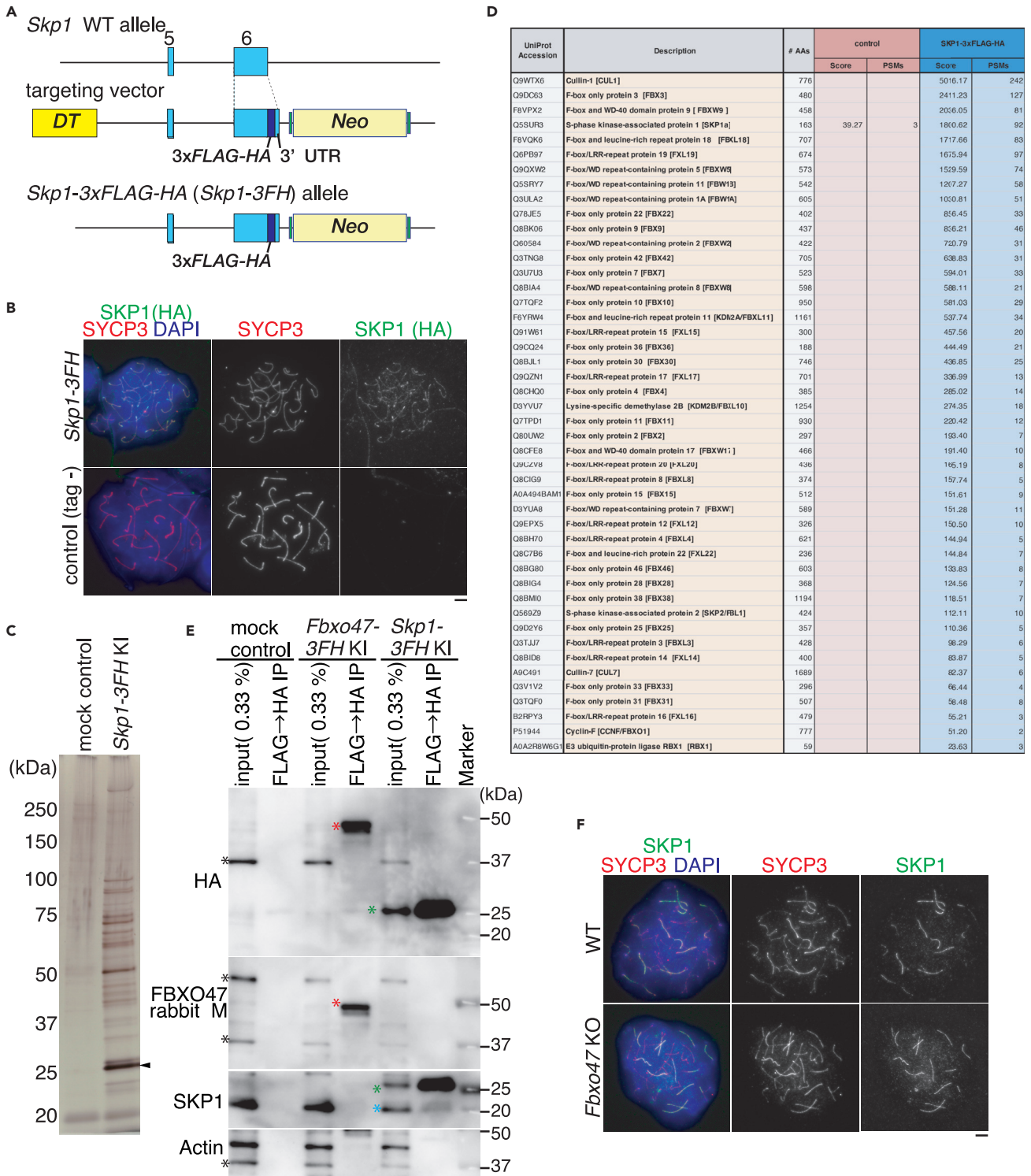
Figure 2. Lack of detection of FBXO47-SKP association in testes by immunoprecipitation

(A) Schematic illustrations of the *Skp1-3xFLAG-HA* knock-in (*Skp1-3FH* KI) allele. Blue boxes represent exons. The stop codon in the exon six was replaced with in-frame *3xFLAG-HA* and the endogenous 3′UTR.

(B) Chromosome spreads of WT (untagged) and *Skp1-3FH* KI spermatocytes were immunostained as indicated. Scale bar: 5 μm.

(C) Silver staining of the immunoprecipitates from cytosolic extracts of WT (untagged control) and *Skp1-3FH* KI mouse testes (14–21-day-old) after tandem affinity purifications using anti-FLAG and anti-HA antibodies. Arrowhead: SKP1-3xFLAG-HA.

Figure 2. _Continued_

(D) The immunoprecipitates from the cytosolic fraction of the WT (untagged control) and _Skp1-3FH_ KI testis extracts were subjected to liquid chromatography-tandem mass spectrometry (LC-MS/MS) analyses. The Fbox-containing proteins and SCF subunits identified by the LC-MS/MS analysis are presented after excluding the proteins detected in the control mock purification. The proteins are listed with SwissProt accession number, the number of peptide hits, and Mascot scores. Full list of identified proteins are shown in the Data S1. It is worth noting that SC central element components, Six6OS1 and SYCE1, were included in the LC-MS/MS data of SKP1-3xFLAG-HA immunoprecipitates (Data S1). This suggests that SCF E3 ubiquitin ligase may target those SC components using an F box protein listed in the LC-MS/MS data as a substrate recognition subunit.

(E) Western blot showed immunoprecipitates from cytosolic extracts of WT (untagged control), _Fbxo47-3FH_ KI and _Skp1-3FH_ KI (heterozygous) testes (14–21-day-old) after tandem affinity purifications using anti-FLAG and anti-HA antibodies. The same membrane was sequentially reblotted with different antibodies as indicated. Red *: FBXO47-3xFLAG-HA, Green *: SKP1-3xFLAG-HA, Blue *: endogenous SKP1, Black *: nonspecific band. Note that SKP1 was not detected in FBXO47 immunoprecipitate from _Fbxo47-3FH_ KI testis extracts, and reciprocally FBXO47 was not detected in SKP1 immunoprecipitate from _Skp1-3FH_ KI testis extracts.

(F) Chromosome spreads of WT and _Fbxo47_ KO spermatocytes were immunostained as indicated. Scale bar: 5 μm.

with a previous study (Chen et al., 2018). Reanalysis of previous scRNA-seq data of fetal ovaries (Shimada et al., 2021) suggested that _Fbxo47_ mRNA was expressed upon _Stra8_ activation in a similar timing as that of _Dmc1_ in the ovaries (Figure 1E). Furthermore, RT-qPCR analysis demonstrated that expression of _Fbxo47_ mRNA culminated at E16.5 and declined afterward in the ovary (Figure 1F).

To determine the meiotic stage-specific expression of FBXO47 protein, we generated different antibodies against FBXO47 C-terminal region (aa 271–451) and middle region (aa173-316). However, we failed to evaluate stage specificity of endogenous FBXO47 protein expression by immunostaining, although it was uncertain whether this was because of the sensitivity of the antibodies, inaccessibility of the antibodies to the epitopes, or low expression level of FBXO47 protein in the target cells.

To circumvent this issue, we generated _Fbxo47-3xFLAG-HA_ knock-in (_Fbxo47-3FH_ KI) mice, which allowed the detection of FBXO47-3xFLAG-HA protein expressed from endogenous _Fbxo47_ locus (Figures 1G and S1). We examined FBXO47-3xFLAG-HA fusion protein from cytosolic and chromatin extracts of _Fbxo47-3FH_ KI testes. Immunoblotting demonstrated that FBXO47 protein was detected with FLAG antibody only when it was enriched by tandem immunoprecipitations using anti-FLAG and anti-HA antibodies (Figure 1H), suggesting that the expression level of FBXO47 protein was low in testes. We noticed that more FBXO47 protein was detected in the cytosolic fraction compared to the chromatin fraction (Figure 1H), suggesting its predominant localization in the cytoplasm rather than on the chromatin. Sequential reblotting showed that different antibodies against the endogenous FBXO47 protein that we generated detected the same protein as indicated by anti-FLAG antibody (Figure 1H).

In summary, FBXO47 is expressed presumably at a low level in meiotic prophase I.

Lack of detection of FBXO47-SKP association in testes by immunoprecipitation

FBXO47 possesses a putative Fbox domain, whose biological function has remained elusive. It is well known that Fbox-domain containing proteins confers substrate specificity to SCF (SKP1–Cullin–F-box) E3 ubiquitin ligase (Jin et al., 2004), and 69 different Fbox proteins are estimated to be encoded in the human genome (Reitsma et al., 2017). This prompted us to examine whether SKP1, a major core subunit of SCF, was co-immunoprecipitated with FBXO47 by immunoblot and mass spectrometry analysis (Figures 1H and S2). However, we failed to detect SKP1 in FBXO47 immunoprecipitates.

To further examine whether FBXO47 serves as a subunit of SCF by reciprocal immunoprecipitation of SKP1, we generated _Skp1-3xFLAG-HA_ knock-in (_Skp1-3FH_ KI) mice, which allowed the detection of SKP1-3xFLAG-HA protein expressed from endogenous _Skp1_ locus and its associated factors (Figure 2A). Although the homozygous _Skp1-3xFLAG-HA_ KI mice were embryonic lethal, heterozygous knock-in mice were fertile and developed normally. Consistent with a previous study (Guan et al., 2020), although SKP1-3xFALG-HA fusion protein localized along the SC in the _Skp1-3FH_ KI spermatocytes (Figure 2B), FBXO47 protein did not show such a specific localization pattern on the chromosome (Figure S3B). SKP1-3xFLAG-HA was enriched by tandem immunoprecipitations using anti-FLAG and anti-HA antibodies from testis cytosolic fraction (Figure 2C). Mass spectrometry analysis demonstrated that total of 45 different Fbox-domain containing proteins and SCF core subunits (SKP1, RBX1, CUL1, and CUL7) were co-immuno-precipitated with SKP1-3xFLAG-HA (Figure 2D, Data S1). However, we failed to detect FBXO47 in the SKP1-3xFLAG-HA immunoprecipitates either by mass spectrometry analysis or by western blotting (Figures 2D and 2E). SKP1 localized along the SC in _Fbxo47_ KO, suggesting that localization of SKP1 did
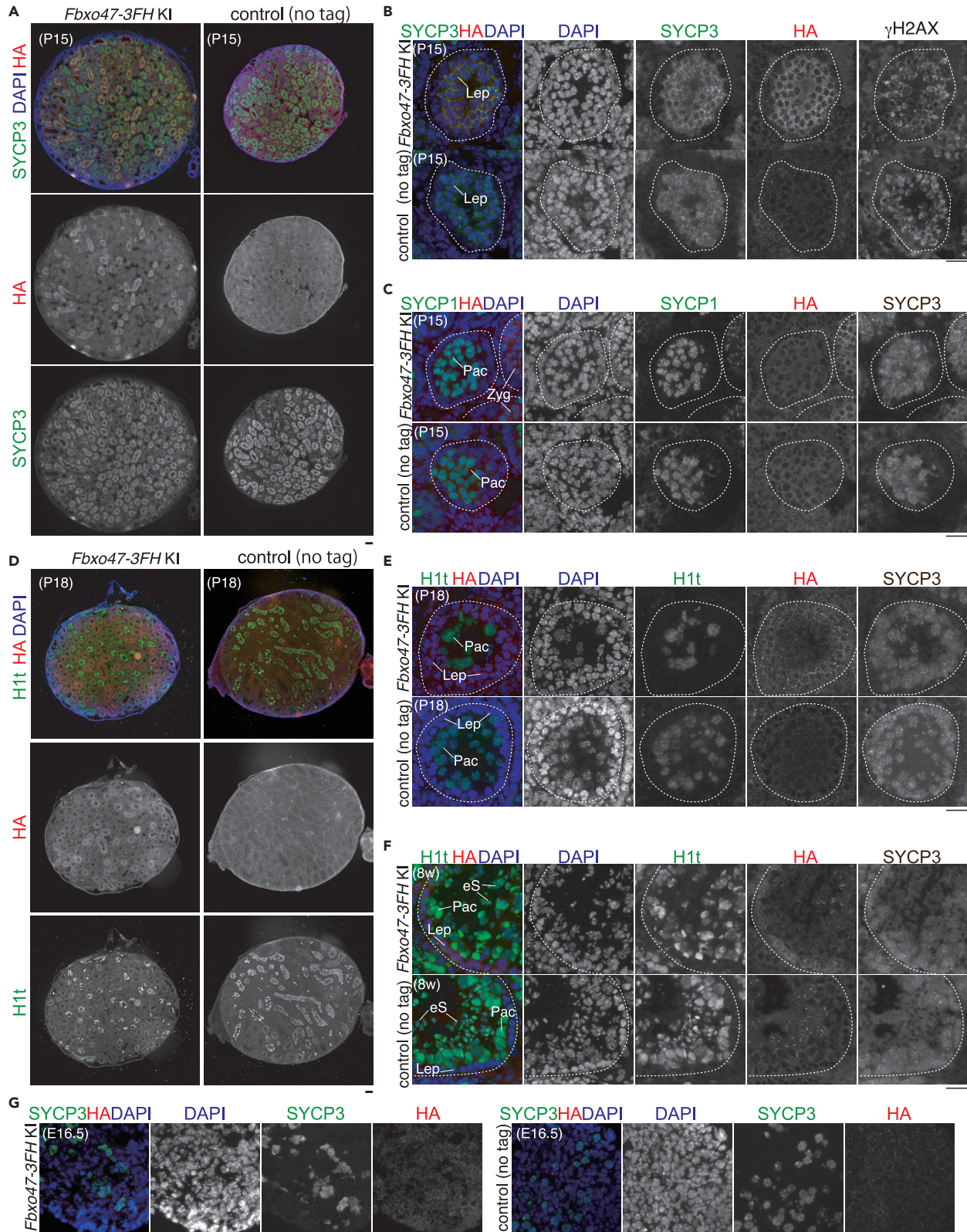
Figure 3. FBXO47 was expressed in early meiotic prophase I in the testis

(A) Testis sections from *Fbxo47-3FH* KI and control (untagged) mice (P15) were stained for HA, SYCP3, and DAPI. Average 21% of the seminiferous tubules that have SYCP3+ spermatocytes showed HA+/SYCP3+ in *Fbxo47-3FH* KI testes (n = 3 animals), whereas none of those was HA+/SYCP3+ in WT (n = 3 animals). Scale bar: 100 μm.

(B) Seminiferous tubule sections from *Fbxo47-3FH* KI and control (untagged) mice (P15) were stained for HA, SYCP3, γH2AX, and DAPI. Lep: leptotene. Scale bar: 25 μm.

(C) Seminiferous tubule sections were stained for HA, SYCP3, SYCP1, and DAPI as in (B). Zyg: zygotene, Pac: pachytene spermatocyte, rS: round spermatid, eS: elongating spermatid. Scale bar: 25 μm.

(D) Testis sections from *Fbxo47-3FH* KI and control (untagged) mice (n = 3 for each genotype, P18) were stained for HA, H1t, and DAPI as in (A). Number of seminiferous tubules that have HA+/H1t + cells was counted per the seminiferous tubules that have H1t + spermatocyte cells (52, 36, 18 tubules for untagged control; 15, 51, 36 tubules for *Fbxo47-3FH* KI mice). Scale bar: 100 μm.

(E) Seminiferous tubule sections (P18) were stained for HA, SYCP3, H1t, and DAPI as in (B). Lep: leptotene, Pac: pachytene spermatocyte, rS: round spermatid, eS: elongating spermatid. Scale bar: 25 μm.

(F) Seminiferous tubule sections (8-weeks old) were immunostained as in (E). Lep: leptotene, Pac: pachytene spermatocyte, eS: elongating spermatid. Scale bar: 25 μm. Note that pachy signals of HA immunostaining were nonspecific , because they were visible in control.

(G) Embryonic ovary sections (E16.5) were immunostained as indicated. Scale bar: 25 μm.

not depend on FBXO47 (Figure 2F). Altogether, our data suggest that FBXO47 may function independently of SCF in mouse testes. Previous study showed that FBXO47 interacts with SKP1 in yeast two-hybrid assay and in GFP-SKP1 IP using HEK293T cell extract that overexpressed FLAG-FBXO47 and GFP-SKP1 (Hua et al., 2019). We do not know the exact reason for these controversial observations between our present study and the previous one (Hua et al., 2019). This could be because of their detection methodology using yeast and overexpression of FBXO47 in culture cells and/or technically limited sensitivity of our detection by immunoprecipitation, because the expression level of FBXO47 protein was low in spermatocytes.

Expression of FBXO47 is limited to early meiotic prophase I in mouse testes

To identify the specific stage in which FBXO47 was expressed, we performed immunostaining using stage specific markers SYCP3 (a component of meiotic chromosome axis), SYCP1 (a marker of homologous chromosome synapsis), and γH2AX (a marker of DSBs). Immunostaining of the *Fbxo47-3FH* KI testis (P15) indicated that FBXO47 protein was detected by HA antibody in average 21% (n = 3) among total SYCP3 positive seminiferous tubules (Figure 3A). Close inspection of seminiferous tubules showed that FBXO47 protein indicated by the presence of HA staining appeared in the cytosol at leptotene and zygotene (Figures 3B and 3C). Notably, the expression level of FBXO47-3xFLAG-HA fusion protein declined in pachytene, when homologs were fully synapsed (Figure 3C). Testis-specific histone H1t is a marker of spermatocytes later than mid pachytene (Cobb et al., 1999; Drabent et al., 1996). Immunostaining of seminiferous tubules by testis-specific histone H1t indicated that FBXO47 protein was expressed only in the H1t negative stage (Figure 3D). None of H1t positive spermatocytes showed FBXO47 immunostaining (Figure 3E), suggesting that FBXO47 expression had declined by mid-pachytene. Thus, the expression of FBXO47 protein was limited to a narrow window of early meiotic prophase I. Although the expression of *Fbxo47* mRNA was upregulated in spermatids, immunostaining of FBXO47 protein detected no more than background levels in spermatids (Figure 3F). This suggested that the expression of FBXO47 might be posttranscriptionally suppressed after postmeiotic spermatids to have the expression specifically limited to early meiotic prophase I. Furthermore, although the expression of *Fbxo47* mRNA was detected in ovaries at E16.5, immunostaining of FBXO47 protein detected no more than background levels in ovaries (Figure 3G).

Disruption of *Fbxo47* led to severe defect in spermatogenesis

To address the role of *Fbxo47* in meiosis, we deleted Exon3-Exon11 of *Fbxo47* loci in C57BL/6 fertilized eggs through the CRISPR/Cas9 system (Figure 4A). RT-PCR analysis showed that *Fbxo47* mRNA expression level was absent in *Fbxo47* KO testis (Figure 4B). Although *Fbxo47* KO male mice did not show overt phenotype in somatic tissues, defects in male reproductive organs were evident with smaller-than-normal testes (Figure 4C). Histological analysis revealed that postmeiotic spermatids and spermatozoa were absent in eight-week-old *Fbxo47* KO seminiferous tubules (Figure 4D). Accordingly, sperm was absent in adult *Fbxo47* KO caudal epididymis (Figure 4E). Consistently, seminiferous tubules that contain PNA lectin (a marker of spermatids) positive cells were absent in *Fbxo47* KO (Figure 4F). Thus, the later stage of spermatogenesis was severely abolished in *Fbxo47* KO seminiferous tubules, resulting in male infertility (Figure 4G). In contrast to male, *Fbxo47* KO females exhibited seemingly normal fertility with no apparent defects in adult ovaries (Figure 4H). Consistent with this histological observation of ovaries, metaphase I
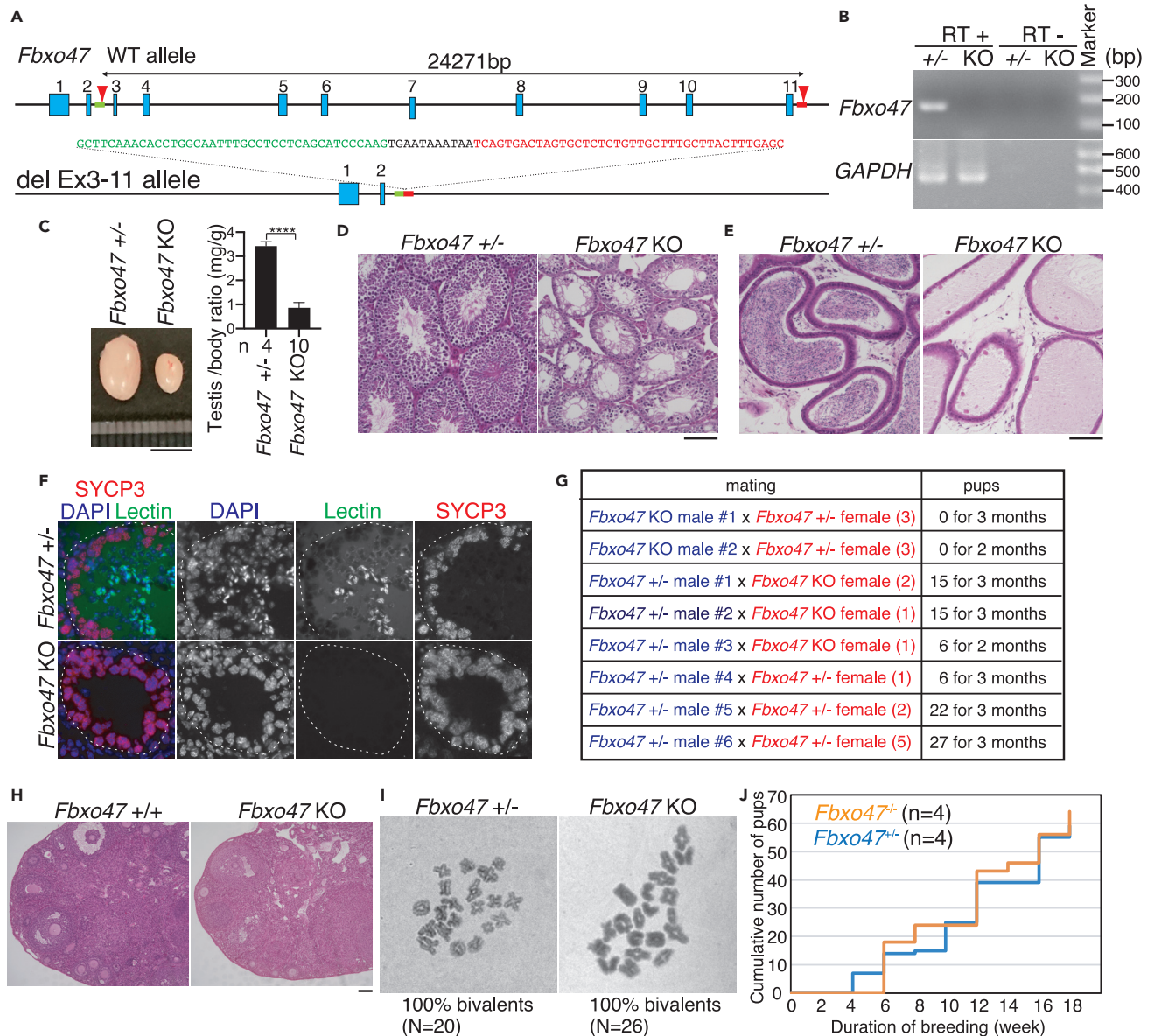
Figure 4. Spermatogenesis was impaired in *Fbxo47* knockout male

(A) The allele with targeted deletion of Exon3-13 in *Fbxo47* gene was generated by the introduction of CAS9, the synthetic gRNAs designed to target intron2 and the downstream of Exon11 (arrowheads), and ssODN (green and red boxes) into C57BL/6 fertilized eggs.

(B) *Fbxo47* mRNA expression was examined by RT-PCR. Testis RNA was obtained from *Fbxo47*^{+/−} and *Fbxo47* KO males (P13). RT-indicates control PCR without reverse transcription.

(C) Testes from *Fbxo47*^{+/−} and *Fbxo47* KO (8-weeks old). Testis/body-weight ratio (mg/g) of *Fbxo47*^{+/−} and *Fbxo47* KO mice (8-weeks old) is shown on the right (Mean with SD). n: the number of animals examined. Statistical significance is shown by ****: $p < 0.0001$ (Two-tailed t-test). Scale bar: 5 mm.

(D) H&E staining of the sections from *Fbxo47*^{+/−} and *Fbxo47* KO testes (8-weeks old). Biologically independent mice for each genotype were examined. Scale bar: 100 μm.

(E) H&E staining of the sections from *Fbxo47*^{+/−} and *Fbxo47* KO epididymis (8-weeks old). Biologically independent mice for each genotype were examined. Scale bar: 100 μm.

(F) Seminiferous tubule sections (8-weeks old) were stained for SYCP3, PNA lectin, and DAPI. Note that the seminiferous tubule that contained PNA-positive elongated spermatids were not identified in *Fbxo47* KO testes. Scale bar: 25 μm.

(G) Number of pups born by mating *Fbxo47*^{+/−} and *Fbxo47* KO males with *Fbxo47*^{+/−} or *Fbxo47* KO females (N = number of females in the same cage) to examine fertility. *Fbxo47* KO male #1 was initially mated with three *Fbxo47*^{+/−} females (all 6-weeks old at the start point of mating). After one month, another *Fbxo47* KO male #2 started to cohabit with those females (8-weeks old at the start point of mating). This cage was observed for 3 months from the start of mating.

Figure 4. *Continued*

(H) H&E stained sections of *Fbxo47*^{+/−} and *Fbxo47* KO ovaries (8-weeks old). Scale bar: 100μm.

(I) Giemsa staining of metaphase I chromosomes from *Fbxo47*^{+/−} (N = 20) and *Fbxo47* KO spermatocytes (N = 26).

(J) Cumulative number of pups born from *Fbxo47*^{+/−} (n = 4, all 6-weeks old at the start point of mating) and *Fbxo47* KO (n = 4, all 6-weeks old at the start point of mating) females.

oocytes derived from *Fbxo47* KO females processes normal number of bivalent chromosomes with chiasmata, indicating that *Fbxo47* KO oocytes had progressed normal meiotic prophase I (Figure 4I). Furthermore, *Fbxo47* KO females were fertile (Figures 4G and 4J), although we could not exclude the possibility that more subtle defects might have occurred in the ovaries besides fertility. Thus, the infertility caused by disruption of *Fbxo47* was male specific. Therefore, these results suggest that requirement of FBXO47 is sexually different in mouse.

Synaptonemal complex was prematurely disassembled in *Fbxo47* KO spermatocytes

To further investigate at which stage the primary defect appeared in the *Fbxo47* KO, we analyzed the progression of spermatogenesis by immunostaining. Testis-specific histone H1t is a marker of spermatocytes later than mid pachytene and round spermatids (Cobb et al., 1999; Drabent et al., 1996). Close inspection of the seminiferous tubules (3 weeks) by immunostaining with antibodies against H1t along with SYCP3 (a component of meiotic chromosome axis) indicated that *Fbxo47* KO spermatocytes failed to reach mid pachytene, whereas spermatocytes in age-matched control passed beyond mid pachytene as indicated by the presence of H1t staining (Figure 5A). This suggests that progression of meiotic prophase I was blocked in *Fbxo47* KO spermatocytes. Immunostaining analysis of spread chromosome with antibodies against SYCP3 along with SYCP1 (a marker of homolog synapsis) demonstrated that *Fbxo47* KO spermatocytes underwent homologous chromosome synapsis and seemingly reached pachytene stage as in age-matched control (Figure 5B).

Curiously, however, *Fbxo47* KO spermatocytes exhibited apparent diplotene-like chromosome morphology (Figure 5B), despite the failure in reaching H1t positive mid pachytene (Figure 5A). It should be mentioned that in the diplotene-like *Fbxo47* KO spermatocytes, SYCP3-stained axes do not show thickening at the telomere ends, although it should typically be observed in late pachytene and diplotene chromosomes of spermatocytes.

It is known that homolog synapsis is initiated at interstitial regions on the chromosome arm at zygotene, and that desynapsis of homologs first starts at interstitial regions on the chromosome arm, whereas telomere regions are prone to be the last place of desynapsis at diplotene (Bisig et al., 2012; Qiao et al., 2012). This cytological difference readily distinguishes desynpased chromosomes at diplotene from unsynapsed ones at zygotene. Indeed, those *Fbxo47* KO spermatocytes with diplotene-like chromosome morphology apparently showed a typical feature of desynapsis of homologs, wherein telomere regions retained homolog synapsis while interstitial regions were free from synapsis. To solve the paradox that *Fbxo47* KO spermatocytes showed diplotene-like chromosome morphology despite the failure of progressing beyond H1t-positive pachytene stage, we further analyzed the meiotic prophase I population at P15 and P18 in the first wave of spermatogenesis of *Fbxo47* KO testes. It should be mentioned that more zygotene and reciprocally less pachytene populations were observed in *Fbxo47* KO spermatocytes compared to WT at P15 and P18 (Figure 5C). This implies that the process of homolog synapsis, at least in part, may be delayed in *Fbxo47* KO spermatocytes as has been shown previously (Hua et al., 2019).

Notably, "diplotene-like" cells (6.7%) appeared in *Fbxo47* KO spermatocytes as early as P15, whereas the first wave of spermatogenesis was yet to pass beyond pachytene stage in the age-matched WT (Figure 5C). HORMAD1 localizes along unsynapsed chromosomes before pachytene and desynapsed chromosomes at diplotene, but dissociates from synapsed chromosomes (Daniel et al., 2011; Shin et al., 2010; Wojtasz et al., 2009). In *Fbxo47* KO spermatocytes, HORMAD1 dissociated from synapsed chromosomes at pachytene and re-localizes on desynapsed chromosomes at diplotene-like stage as in those of WT (Figure 5D), suggesting that localization of HORMAD1 on chromosomes was normally regulated. Histone H3 Ser10 phosphorylation (H3S10p) by Aurora B kinase of the chromosome passenger complex marks the centromeric region at diplotene and the whole chromosome at metaphase I (Parra et al., 2003, 2009). In the control spermatocytes, the centromeric regions at diplotene were indicated by immunostaining of H3S10p (Figure 5E). In contrast, H3S10p-positive centromeric regions were not observed in *Fbxo47* KO diplotene-like spermatocytes (Figure 5E). This observation indicated that *Fbxo47* KO spermatocytes failed
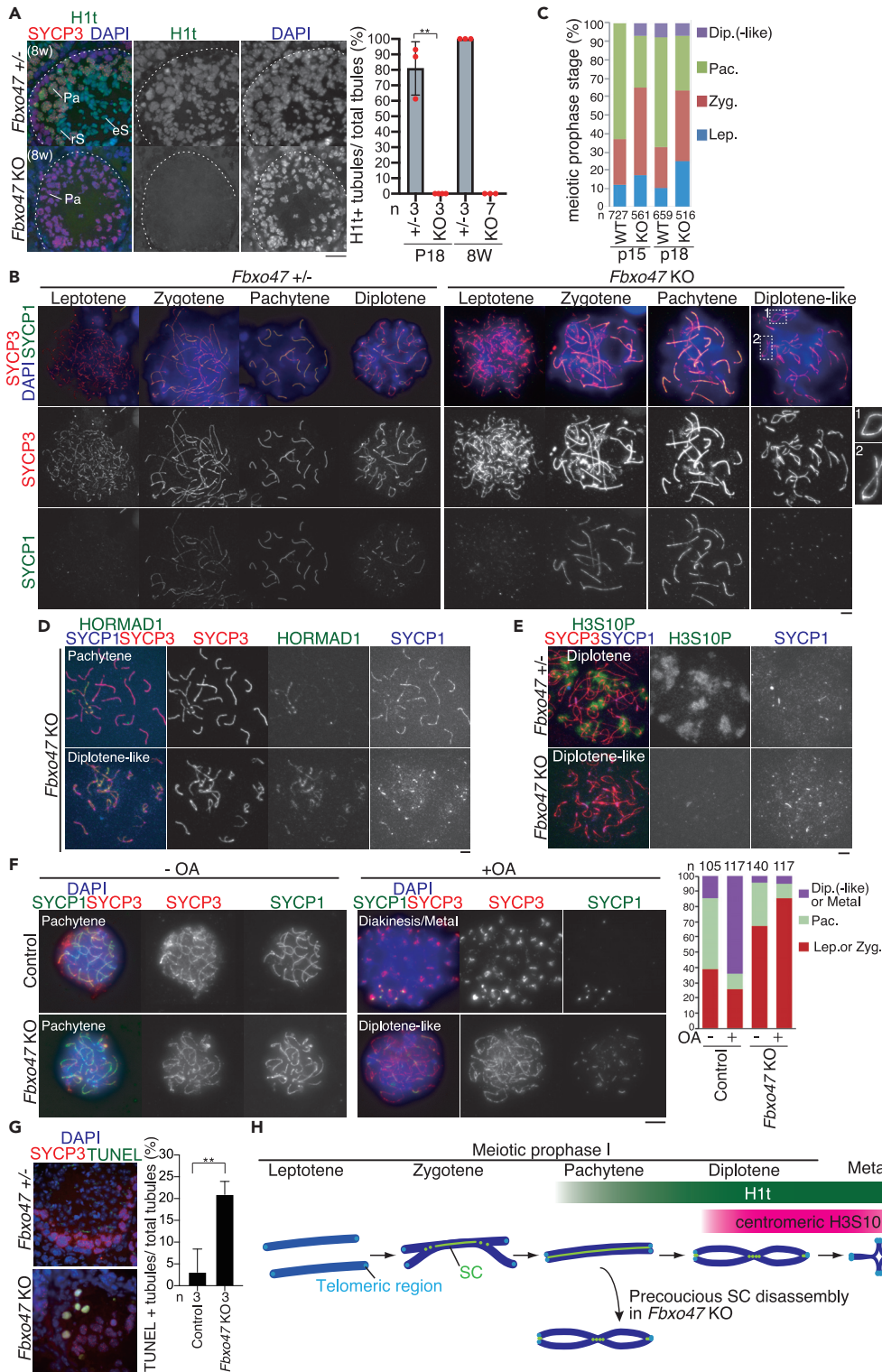
Figure 5. Premature disassembly of SC in *Fbxo47* KO spermatocytes

Figure360▷ For a Figure360 author presentation of this figure, see https://doi.org/10.1016/j.isci.2022.104008.

(A) Seminiferous tubule sections (P18 and 8-weeks old) were stained for SYCP3, H1t, and DAPI. Pa: pachytene spermatocyte, rS: round spermatid, eS: elongating spermatid. Shown on the right is the quantification of the seminiferous tubules that have H1t+/SYCP3+ cells per the seminiferous tubules that have SYCP3+ spermatocyte cells in WT and

Figure 5. *Continued*

Fbxo47 KO mice (Mean with SD). n: the number of animals examined for each genotype. Statistical significance is shown (Unpaired t test). **: p = 0.0012 for *Fbxo47* heterozygous versus *Fbxo47* KO at P18. *Fbxo47* heterozygous (p18: 62, 61, 29 tubules/animal were counted from three animals; 8w: 135, 143, 45 tubules/animal were counted from three animals) and *Fbxo47* KO testes (p18: 105, 59, 141 tubules/animal were counted from three animals; 8w: 36, 55, 63, 64, 88, 69, 108 tubules/animal were counted from 7 animals). Scale bar: 25 μm.

(B) Chromosome spreads of WT and *Fbxo47* KO spermatocytes (3-4 weeks old) were immunostained as indicated. Enlarged images are shown to highlight desynapsed chromosomes in diplotene-like *Fbxo47* KO spermatocytes. Scale bar: 5 μm.

(C) Quantification of meiotic prophase I stage spermatocytes per total SYCP3+ spermatocytes in WT and *Fbxo47* KO mice at P15 and P18 is shown. n: the number of cells examined.

(D) Chromosome spreads of pachytene and diplotene-like *Fbxo47* KO spermatocytes were immunostained for SYCP3, H3S10P, and HORMAD1. Scale bar: 5 μm.

(E) Chromosome spreads of diplotene spermatocyte in the control and diplotene-like spermatocytes in *Fbxo47* KO spermatocytes (P18) were immunostained for SYCP3, H3S10P, and DAPI. Scale bar: 5 μm. Note that centromeric regions are positively stained for H3S10P in the control diplotene spermatocyte but not in diplotene-like spermatocyte in *Fbxo47* KO spermatocytes.

(F) Spermatocytes isolated from the control $Fbxo47^{+/-}$ and *Fbxo47* KO testes (P18) were cultured *in vitro* in the presence or absence of OA for 3 h. Quantification of meiotic prophase I stage is shown on the right. n: the number of cells examined. Note that the control spermatocytes showed a typical feature of diakinesis/Meta I with condensed chromosomes and remaining SYCP3 at centromeres.

(G) Seminiferous tubule sections from 8-weeks old mice were subjected to TUNEL assay with immunostaining for SYCP3. L: leptotene, Pa: pachytene. Shown on the right is the quantification of the seminiferous tubules that have TUNEL + cells per total tubules in $Fbxo47^{+/-}$ (8w; n = 3) and *Fbxo47* KO (8w; n = 3) testes (mean with SD). Statistical significance is shown by **p = 0.0072 (Two-tailed t-test). Scale bar: 25 μm.

(H) Schematic illustration of the precocious SC disassembly observed in *Fbxo47* KO spermatocytes. The expression timing of H1t and H3S10P markers is shown.

to reach *bona fide* diplotene stage of meiotic prophase I, albeit exhibiting apparent homolog desynapsis. Thus, we reasoned that even though homolog synapsis once occurred, it was destabilized during pachytene in *Fbxo47* KO spermatocytes. Altogether, FBXO47 plays a negative role in desynapsis or FBXO47 is required for stability of synapsis.

Mid-late pachytene spermatocytes acquire competency for meiotic prophase-Metaphase I transition indicted by the response to phosphatase inhibitor okadaic acid (OA) (Cobb et al., 1999). *In vitro* culture of isolated spermatocytes in the absence or presence of OA demonstrated that although the control spermatocytes progressed to diakinesis/metaphase I in the presence of OA, *Fbxo47* KO spermatocytes did not (Figure 5F). Because *Fbxo47* KO spermatocytes were yet to acquire competency for OA-induced progression into metaphase I, even the most advanced *Fbxo47* KO spermatocytes remained in an earlier cell cycle stage compared to the control. These results suggested that the primary defect occurred at zygotene or early pachytene stage in *Fbxo47* KO spermatocytes. Notably, TUNEL positive cells were observed in ~21% of *Fbxo47* KO seminiferous tubules (Figure 5G), suggesting that *Fbxo47* KO spermatocytes were consequently eliminated by apoptosis. Altogether, these results suggested that SC was prematurely disassembled in *Fbxo47* KO spermatocytes (Figure 5H).

Fbxo47 KO spermatocytes show defects in meiotic recombination

Aforementioned results suggested that FBXO47 protein was required for stable maintenance of SC (Figure 5). SC facilitates meiotic recombination that is executed by DSB formation and repair steps. Then SC is disassembled after the completion of crossover formation. Given that SC was prematurely destabilized in *Fbxo47* KO spermatocytes, we assumed two possibilities: (1) premature SC disassembly could be a result of early completion of meiotic recombination. (2) premature SC disassembly abolished the processes of meiotic recombination. To address these issues, we examined DSB formation, repair events, and meiotic silencing of unsynapsed chromatin (MSUC) by immunostaining of γH2AX. The first wave of γH2AX is mediated by ATM after DSB formation at leptotene (Mahadevaiah et al., 2001) and disappears during DSB repair. The second wave of γH2A at zygotene is mediated by ATR that targets unsynapsed chromosomes (Royo et al., 2013). At zygotene, γH2AX signal appeared in *Fbxo47* KO spermatocytes in the same manner as WT (Figure 6A), indicating that DSB formation normally occurred in *Fbxo47* KO spermatocytes. However, γH2AX signals largely persisted throughout the nuclei until pachytene-like and diplotene-like stages in *Fbxo47* KO spermatocytes, whereas they overall disappeared in WT pachytene spermatocytes except for retaining on the XY body (Figure 6A). This observation suggested that DSBs
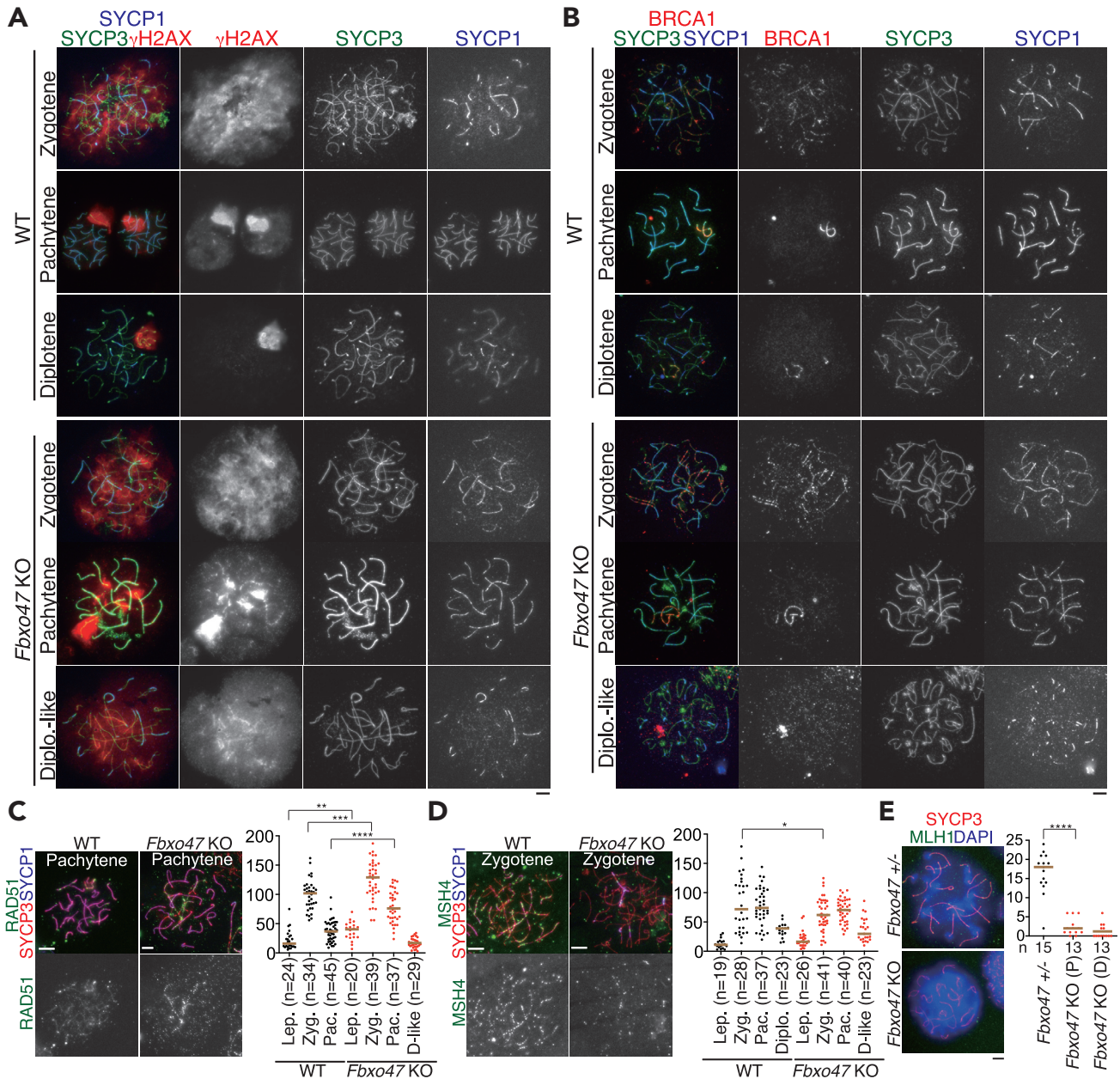
Figure 6. *Fbxo47* **KO spermatocytes show defects in meiotic recombination**

(A) Chromosome spreads of WT and *Fbxo47* KO spermatocytes (P18) were immunostained for SYCP3, SYCP1, and γH2AX.

(B) Chromosome spreads of WT and *Fbxo47* KO spermatocytes (P18) were immunostained for SYCP3, SYCP1, and BRCA1.

(C) Chromosome spreads of WT and *Fbxo47* KO spermatocytes were stained as indicated. Immunostained chromosome spread of pachytene spermatocytes is shown. The number of RAD51 foci is shown in the scatterplot with median (right). Statistical significance is shown by p value (Mann-Whitney U-test). ****: p < 0.0001. ***: p < 0.001. **: p < 0.01. Lep.: leptotene, Zyg.: Zygotene, Pac.: Pachytene, Z-like: Zygotene-like, P-like: Pachytene-like, D-like: Diplotene-like. n: the number of cells examined. Data were pooled from two to three animals at P18.

(D) Chromosome spreads of WT and *Fbxo47* KO spermatocytes were stained as indicated. The number of MSH4 foci is shown in the scatterplot with median (right). Statistical significance is shown by p value (Mann-Whitney U-test). *: p < 0.05. Data were pooled from two to three animals at P18.

(E) Chromosome spreads of *Fbxo47*^{+/−} and *Fbxo47* KO spermatocytes (P18) were stained as indicated. The number of MLH1 foci is shown in the scatterplot with median (right). Statistical significance is shown by p value (Mann-Whitney U-test). ***: p < 0.0001. Scale bars: 5 μm.

were still not repaired and/or newly generated in *Fbxo47* KO spermatocytes. Alternatively, γH2AX signals newly appeared in response to MSUC in *Fbxo47* KO spermatocytes. This may imply at least in part that homolog synapsis was partly incomplete in *Fbxo47* KO spermatocytes, as suggested by more zygotene

and reciprocally less pachytene populations in *Fbxo47* KO (Figure 5C). Notably, XY body was not detectable in *Fbxo47* KO pachytene and diplotene-like spermatocytes, suggesting that FBXO47 is directly or indirectly required for XY body formation. Furthermore, BRCA1, a marker of asynapsis (Broering et al., 2014; Scully et al., 1997; Turner et al., 2004), appeared along unsynapsed autosomal axes in zygotene *Fbxo47* KO spermatocytes as in those of WT (Figure 6B). This suggests that MSUC was normally activated in *Fbxo47* KO spermatocytes. Crucially, in contrast to unsynapsed chromosomes in zygotene, BRCA1 was not observed along precociously desynapsed chromosomes in *Fbxo47* KO diplotene-like spermatocytes (Figure 6B). This suggests that MSUC was canceled in *Fbxo47* KO diplotene-like spermatocytes, presumably once homolog synapsis had successfully been achieved.

RAD51 facilitates the invasion of 3′-extended strand into the duplex of homolog at DSBs (Cloud et al., 2012; Shinohara and Shinohara, 2004). In *Fbxo47* KO, the number of RAD51 foci was significantly increased in *Fbxo47* KO spermatocytes at leptotene and zygotene (Figure 6C). Although we do not know the exact reason for the increase of RAD51 foci at leptotene in *Fbxo47* KO, this may imply that more DSBs were generated. Reciprocally, the number of MSH4 foci was decreased in *Fbxo47* KO zygotene spermatocytes (Figure 6D). These observations suggest that although RAD51 was normally loaded onto DSBs, the processes of homologous recombination-mediated repair were delayed in the absence of FBXO47. Accordingly, the number of MLH1 foci, a marker of crossover (CO) that should appear in mid to late pachytene spermatocytes, was significantly reduced in *Fbxo47* KO pachytene-like spermatocytes compared to WT pachytene spermatocytes (Figure 6E). This further implies that spermatocytes were yet to reach *bona fide* mid to late pachytene in the absence of FBXO47. Altogether, precocious disassembly of SC was a cause of the defect in meiotic recombination rather than a result of early completion of meiotic recombination.

Previous study showed that mouse FBXO47 interacts with SKP1 and telomere binding proteins, TRF1 and TRF2, and *Fbxo47* KO spermatocytes showed defects in telomere bouquet formation (Hua et al., 2019), which were different to the observations in the present study (Figures S3A–S3C). This could be in part because of detection sensitivity or different epitope recognition of different antibodies. Because the frequency of bouquet formation was quite low even in WT spermatocytes in mouse (Figure S3D), as shown in our previous study (Ishiguro et al., 2014), the potential defect in bouquet formation in *Fbxo47* KO spermatocytes further needs to be evaluated. Although we do not know the exact reason for the different observations in *Fbxo47* KO testes, subtle differences in the detection and assay conditions or mice that were used could account for the differences in the observations.

DISCUSSION

FBXO47 stabilizes homolog synapsis in mouse

We have shown that FBXO47 is required for the maintenance of homolog synapsis during prolonged meiotic prophase I in male. Previous study found that any spermatocytes that progressed beyond zygotene were not found in *Fbxo47* KO (Hua et al., 2019). Although partly agreeing with their interpretation, in the present study, *Fbxo47* KO spermatocytes failed to progress beyond the *bona fide* pachytene stage of meiotic prophase I in terms of cell cycle status. The present study rather suggest that homologs were prematurely desynapsed in *Fbxo47* KO spermatocytes, albeit the existence of *Fbxo47* KO spermatocytes exhibiting apparent pachytene and diplotene-like chromosome morphologies (Figure 5).

Fbxo47 KO spermatocytes showed precocious desynapsis, albeit exhibiting apparently "diplotene-like" morphology (Figure 5B). Although this phenomenon in *Fbxo47* KO spermatocytes was partly similar to that observed in conditional *Skp1* KO (Guan et al., 2020), marked phenotypic differences were observed between *Fbxo47* KO and *Skp1* KO spermatocytes. In *Skp1* KO testis, late pachytene spermatocytes are absent and concurrently diplotene spermatocytes are increased. *Skp1* KO spermatocytes at least reach H1t positive mid-pachytene in terms of cell cycle, but most of them contain desynapsed chromosomes at pericentric end termed "Y pachynema". Thus, *Skp1* KO spermatocytes show precocious desynapsis and pachytene exit. In contrast, *Fbxo47* KO spermatocytes failed to reach H1t positive mid-pachytene (Figure 5A). Although apparent diplotene-like morphology of homologous chromosomes appeared in *Fbxo47* KO spermatocytes (Figure 5B), "Y pachynema" was not observed in *Fbxo47* KO, unlike in *Skp1* KO spermatocytes. Thus, *Fbxo47* KO spermatocytes show precocious desynapsis despite the

failure of progression beyond pachytene. These results suggested that the primary defect in *Fbxo47* KO spermatocytes occurred at an earlier cell cycle stage than *Skp1* KO spermatocytes. HORMAD1 localizes along unsynapsed and desynapsed chromosomes during meiotic prophase (Daniel et al., 2011; Shin et al., 2010), and dissociates from synapsed chromosomes by the action of TRIP13 AAA ATPase (Wojtasz et al., 2009). Although HORMAD1 persists both in synapsed and desynapsed chromosomes in *Skp1* KO spermatocyte, localization of HORMAD1 on chromosomes was normally regulated in *Fbxo47* KO (Figure 5D). Thus, precocious desynapsis could be derived at least in part from failure of HORMAD1 removal in *Skp1* KO and from a different mechanism in *Fbxo47* KO. Moreover, although the DSB repair process indicated by γH2AX staining (Figure 6A) was impaired both in *Fbxo47* KO and in *Skp1* KO spermatocytes, the extent of crossover formation was different between them. Although significant number of MLH1 foci were observed in mid-late pachytene and diplotene spermatocytes in *Skp1* KO; however, MLH1 foci were rarely observed in pachytene and diplotene-like spermatocytes in *Fbxo47* KO (Figure 6E). Thus, meiotic recombination and crossover formation were more progressed in *Skp1* KO than in *Fbxo47* KO.

We showed sex specific difference in the phenotype of *Fbxo47* KO mice. Although *Fbxo47* is expressed in embryonic ovaries (Figures 1E and 1F), *Fbxo47* KO oocytes had progressed through meiotic prophase I and the *Fbxo47* KO females showed fertility comparable to WT (Figures 4H–4J), which is similar to male-specific meiotic defects observed in previous studies (Takemoto et al., 2020) (Horisawa-Takada et al., 2021). Although we could not exclude the possibility that more subtle defects might have occurred in the *Fbxo47* KO ovaries, this may be at least in part because of strict requirement of FBXO47 for XY body formation during male meiotic prophase I (Figure 6A). Alternatively, because FBXO47 expression was hardly detected at protein level in the embryonic ovaries albeit the expression of *Fbxo47* mRNA (Figure 3G), FBXO47 protein may have a negligible role in females.

Distinct functions of FBXO47 homologs in diverse organisms

Fbxo47 homologues and other distant F box proteins have been implicated in meiotic prophase progression in various species. Although defects accompanying DSB repair and crossover are similarly observed in mouse and *C. elegans Fbxo47* mutants, the primary causes are assumed to be different. In *C. elegans*, PROM-1 encodes *Fbxo47* homolog. In *C. elegans*, organization of gonadal germline is divided into mitotic/meiotic entry zone, transition zone corresponding to zygotene, and pachytene zone. *Prom-1* mutant showed delayed and asynchronous initiation of homolog pairing, so that distinct transition zone was missing and meiotic entry zone was rather extended (Jantsch et al., 2007) with attenuating CHK-2 activity (Antoine et al., 2021; Mohammad et al., 2018). Further, PROM-1 was proposed to down regulate mitotic cell cycle proteins such as Cyclin E homolog CYE-1 at meiotic entry, independently of promoting homolog pairing as a positive regulator of CHK-2 kinase (Mohammad et al., 2018). Thus, PROM-1 functions very early in meiotic prophase in *C. elegans*, which is similar to our observation in mice (Figure 5). In *prom-1* meiocytes, however, homolog pairing was defective and nonhomologous synapsis was consequently pronounced in autosomes but not in X chromosome. Thus, PROM-1 is implicated in promoting autosome homolog pairing. This is a contrast to our observation, in which homolog synapsis once took place normally, followed by premature desynapsis in *Fbxo47* KO spermatocytes (Figure 5B).

In the teleost fish medaka, *fbxo47* mutant XX germ cells exhibit abnormally condensed chromosomes in ovaries and fail to undergo oogenesis after diplotene, showing that the sexual fate of XX germ cells turns into spermatogenesis (Kikuchi et al., 2020). Thus, *fbxo47* is involved in the regulation of cell division in ovaires, and in turn the suppression of spermatogenesis in female germ cells in medaka. The germline feminization under *fbxo47* is mediated at least by two downstream transcription factors *lhx8b* and *figla* during early meiotic prophase in medaka. Despite the phenotypic similarities and differences observed in the mutants of Fbxo47 homologs in diverse organisms, FBXO47 homologs commonly act during meiotic prophase, although at different time points.

Distant F box proteins are involved in homolog synapsis

SCF and F box proteins are involved in the process of homolog synapsis during meiotic prophase I in diverse organisms. In plants, although no *Fbxo47* homologs exist, distant F box proteins are involved in homolog synapsis. In rice plant (*O. sativa*), MEIOTIC F BOX (MOF) encodes an F BOX protein, and interacts
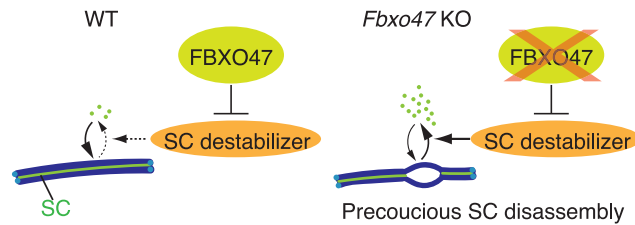
Figure 7. A model of FBXO47 function to prevent premature SC disassembly
Schematic illustration how FBXO47 may protect SC from a putative destabilizer during early meiotic prophase I.

with OSK1, a homolog of SKP1 (He et al., 2016). MOF acts as a subunit of SCF and localizes on the chromosome during meiotic prophase I. In *mof* mutant male meiocytes, telomeres were not clustered and homolog synapsis was lost as indicated by complete absence of ZEP1, a transverse filament of SC. Thus, MOF plays a role in telomere bouquet formation during homolog pairing in male meiocyte. In rice plant, ZYGOTENE1 (ZYGO1) encodes another F box protein that has a limited similarity to mouse FBL12 (Zhang et al., 2017). In *zygo1* mutant, polarized enrichment of OsSAD1, a SUN-domain containing protein, along nuclear envelope was lost and full-length homolog pairing was consequently impaired. This led to defective DSB repair of meiotic recombination, causing both male and female sterility in *zygo1* mutant. Thus, ZYGO1 also plays a role in telomere bouquet formation during homolog pairing in rice plant. These studies suggest that rice F box proteins MOF and ZYGO1 act as an SCF component, and play a role in bouquet formation rather than in the process of SC formation, which is different from the role of mouse FBXO47 in SC maintenance.

In budding yeast, an F box protein Cdc4 acts as a substrate subunit of SCF during meiotic prophase I. SCF ^{Cdc4} is assumed to regulate SC assembly by counteracting the Pch2 (TRIP13 in mammals)-dependent negative action that induces SC disassembly (Zhu et al., 2021). It is proposed that SCF ^{Cdc4} targets the putative negative regulator of SC assembly toward degradation, and in turn stabilizes SC. Although how Pch2 itself or its downstream factors are counteracted by SCF ^{CDC4} remains elusive, F box protein Cdc4 acts for the maintenance of SC in budding yeast.

In *Drosophila* female, knockdown of *SkpA*, a *Skp1* homolog, caused premature disassembly of SC (Barbosa et al., 2021). Depletion of F box proteins, Fbxo42 and Slmb/βTrcp, showed incomplete formation and precocious disassembly of SC, which was similar to the observation in *Fbxo47* KO mouse. PP2A catalytic (C) subunit and structural (A) subunit were identified as a candidate substrate of Fbxo42. Because overexpression of a PP2A subunit Wrd (B56) phenocopied Fbxo42 knockdown, the SCF ^{Fbxo42} is assumed to stabilize SC by restricting PP2A-Wrd (B56) association. In these regards, *Drosophila* Fbxo42 and budding yeast Cdc4 share a similar role to mouse FBXO47 in maintaining SC stability.

Previous studies showed PLK1 mediated-phosphorylation regulate SC disassembly in mouse (Jordan et al., 2012), and PP2A phosphatase inhibitor OA promotes premature exit from pachytene and SC disassembly (Cobb et al., 1999). Thus, phosphorylation level of SC regulates its stability during meiotic cell cycle. Given that FBXO47 exists in the cytosol rather than localizing to the chromatin (Figure 1H), it is possible that FBXO47 may protect the SC directly or indirectly from a putative destabilizer that regulates the phosphorylation level of SC during early meiotic prophase I (Figure 7). It is still a large enigma how FBXO47 acts for preventing premature SC disassembly, and further investigation is required for understanding the precise mechanism of FBXO47 function.

Limitations of study

Although our data showed that FBXO47 was not co-immunoprecipitated with SCF, we cannot exclude the possibility that this was because of the sensitivity of the antibodies, inaccessibility of the antibodies to the epitopes, or low expression level of FBXO47 protein in the spermatocytes. Further, we observed the differences in *Fbxo47* KO phenotypes between our current study and the previous one (Hua et al., 2019), subtle differences in the detection and assay conditions or mice that were used could account for the differences in the observations.

STAR★METHODS

Detailed methods are provided in the online version of this paper and include the following:

- KEY RESOURCES TABLE
- RESOURCE AVAILABILITY
  - Lead contact
  - Materials availability
  - Data and code availability
- EXPERIMENTAL MODEL AND SUBJECT DETAILS
  - Animals
- METHOD DETAILS
  - Generation of *Fbxo47* knockout mice and genotyping
  - Generation of *Fbxo47-3xFLAG-HA* knock-in mice and genotyping
  - Generation of *Skp1-3xFLAG-HA* knock-in mouse and genotyping
  - Histological analysis
  - Immunostaining of spermatocytes
  - Imaging
  - *In vitro* oocyte culture and Giemsa staining of metaphase chromosome spread
  - Culture of OA-induced meta I spermatocyte
  - Antibodies
  - Production of antibodies against FBXO47
  - PCR with reverse transcription
  - Preparation of testis extracts and immunoprecipitation
  - Immuno-affinity purification
  - Mass spectrometry
  - ChIP-seq data and public RNA-seq data analysis
  - Single cell RNA-seq data analysis
- QUANTIFICATION AND STATISTICAL ANALYSIS

SUPPLEMENTAL INFORMATION

Supplemental information can be found online at https://doi.org/10.1016/j.isci.2022.104008.

AUTHOR CONTRIBUTIONS

N.Tanno and K.T. performed the cytological and biochemical analyses. R.S. performed reanalysis of scRNA-seq data. N.Tani performed MS analyses. Y.T.H. performed the RT-PCR. K.A. designed the knockout mice. S.F. performed histological analyses. N.Takeda assisted oocyte experiments. K.I. supervised experiments, conducted the study, and wrote the manuscript.

DECLARATION OF INTERESTS

The authors declare no competing interests.

REFERENCES

Antoine, B., Paouneskou, D., Mohammad, A., Lichtenberger, R., Blundon, J., Kim, Y., Hartl, M., Falk, S., Schedl, T., and Jantsch, V. (2021). The CHK-2 antagonizing phosphatase PPM-1.D regulates meiotic entry via catalytic and non-catalytic activities. Preprint at bioRxiv. https://doi.org/10.1101/2021.08.02.453806.

Barbosa, P., Zhaunova, L., Debilio, S., Steccanella, V., Kelly, V., Ly, T., and Ohkura, H. (2021). SCF-Fbxo42 promotes synaptonemal complex assembly by downregulating PP2A-B56. J. Cell Biol. 220. https://doi.org/10.1083/jcb.202009167.

Baudat, F., Imai, Y., and de Massy, B. (2013). Meiotic recombination in mammals: localization and regulation. Nat. Rev. Genet. 14, 794–806. https://doi.org/10.1038/nrg3573.

Bisig, C.G., Guiraldelli, M.F., Kouznetsova, A., Scherthan, H., Hoog, C., Dawson, D.S., and Pezza, R.J. (2012). Synaptonemal complex components persist at centromeres and are required for homologous centromere pairing in mouse spermatocytes. PLoS Genet. 8, e1002701. https://doi.org/10.1371/journal.pgen.1002701.

Broering, T.J., Alavattam, K.G., Sadreyev, R.I., Ichijima, Y., Kato, Y., Hasegawa, K., Camerini-Otero, R.D., Lee, J.T., Andreassen, P.R., and Namekawa, S.H. (2014). BRCA1 establishes DNA damage signaling and pericentric heterochromatin of the X chromosome in male meiosis. J. Cell Biol. 205, 663–675. https://doi.org/10.1083/jcb.201311050.

Cahoon, C.K., and Hawley, R.S. (2016). Regulating the construction and demolition of the synaptonemal complex. Nat. Struct. Mol. Biol. 23, 369–377. https://doi.org/10.1038/nsmb.3208.

Cardozo, T., and Pagano, M. (2004). The SCF ubiquitin ligase: insights into a molecular machine. Nat. Rev. Mol. Cell Biol. 5, 739–751. https://doi.org/10.1038/nrm1471.

Chen, Y., Zheng, Y., Gao, Y., Lin, Z., Yang, S., Wang, T., Wang, Q., Xie, N., Hua, R., Liu, M., et al. (2018). Single-cell RNA-seq uncovers dynamic processes and critical regulators in mouse spermatogenesis. Cell Res. 28, 879–896. https://doi.org/10.1038/s41422-018-0074-y.

Cloud, V., Chan, Y.L., Grubb, J., Budke, B., and Bishop, D.K. (2012). Rad51 is an accessory factor for Dmc1-mediated joint molecule formation during meiosis. Science 337, 1222–1225. https://doi.org/10.1126/science.1219379.

Cobb, J., Cargile, B., and Handel, M.A. (1999). Acquisition of competence to condense metaphase I chromosomes during spermatogenesis. Dev. Biol. 205, 49–64. https://doi.org/10.1006/dbio.1998.9101.

Daniel, K., Lange, J., Hached, K., Fu, J., Anastassiadis, K., Roig, I., Cooke, H.J., Stewart, A.F., Wassmann, K., Jasin, M., et al. (2011). Meiotic homologue alignment and its quality surveillance are controlled by mouse HORMAD1. Nat. Cell Biol. 13, 599–610. https://doi.org/10.1038/ncb2213.

Deshaies, R.J. (1999). SCF and Cullin/Ring H2-based ubiquitin ligases. Annu. Rev. Cell Dev. Biol. 15, 435–467. https://doi.org/10.1146/annurev.cellbio.15.1.435.

Drabent, B., Bode, C., Bramlage, B., and Doenecke, D. (1996). Expression of the mouse testicular histone gene H1t during spermatogenesis. Histochem. Cell Biol. 106, 247–251. https://doi.org/10.1007/BF02484408.

Guan, Y., Leu, N.A., Ma, J., Chmatal, L., Ruthel, G., Bloom, J.C., Lampson, M.A., Schimenti, J.C., Luo, M., and Wang, P.J. (2020). SKP1 drives the prophase I to metaphase I transition during male meiosis. Sci. Adv. 6, eaaz2129. https://doi.org/10.1126/sciadv.aaz2129.

He, Y., Wang, C., Higgins, J.D., Yu, J., Zong, J., Lu, P., Zhang, D., and Liang, W. (2016). MEIOTIC F-BOX is essential for male meiotic DNA double-strand break repair in rice. Plant Cell 28, 1879–1893. https://doi.org/10.1105/tpc.16.00108.

Hermann, B.P., Cheng, K., Singh, A., Roa-De La Cruz, L., Mutoji, K.N., Chen, I.C., Gildersleeve, H., Lehle, J.D., Mayo, M., Westernstroer, B., et al. (2018). The mammalian spermatogenesis single-cell transcriptome, from spermatogonial stem cells to spermatids. Cell Rep. 25, 1650–1667.e8. https://doi.org/10.1016/j.celrep.2018.10.026.

Horisawa-Takada, Y., Kodera, C., Takemoto, K., Sakashita, A., Horisawa, K., Maeda, R., Shimada, R., Usuki, S., Fujimura, S., Tani, N., et al. (2021). Meiosis-specific ZFP541 repressor complex promotes developmental progression of meiotic prophase towards completion during mouse spermatogenesis. Nat. Commun. 12, 3184. https://doi.org/10.1038/s41467-021-23378-4.

Hua, R., Wei, H., Liu, C., Zhang, Y., Liu, S., Guo, Y., Cui, Y., Zhang, X., Guo, X., Li, W., and Liu, M. (2019). FBXO47 regulates telomere-inner nuclear envelope integration by stabilizing TRF2 during meiosis. Nucleic Acids Res. 47, 11755–11770. https://doi.org/10.1093/nar/gkz992.

Ishiguro, K., Kim, J., Fujiyama-Nakamura, S., Kato, S., and Watanabe, Y. (2011). A new meiosis-specific cohesin complex implicated in the cohesin code for homologous pairing. EMBO Rep. 12, 267–275. https://doi.org/10.1038/embor.2011.2.

Ishiguro, K., Kim, J., Shibuya, H., Hernandez-Hernandez, A., Suzuki, A., Fukagawa, T., Shioi, G., Kiyonari, H., Li, X.C., Schimenti, J., et al. (2014). Meiosis-specific cohesin mediates homolog recognition in mouse spermatocytes. Genes Dev. 28, 594–607. https://doi.org/10.1101/gad.237313.113.

Ishiguro, K.I., Matsuura, K., Tani, N., Takeda, N., Usuki, S., Yamane, M., Sugimoto, M., Fujimura, S., Hosokawa, M., Chuma, S., et al. (2020). MEIOSIN directs the switch from mitosis to meiosis in mammalian germ cells. Dev. Cell 52, 429–445.e10. https://doi.org/10.1016/j.devcel.2020.01.010.

Jantsch, V., Tang, L., Pasierbek, P., Penkner, A., Nayak, S., Baudrimont, A., Schedl, T., Gartner, A., and Loidl, J. (2007). Caenorhabditis elegans prom-1 is required for meiotic prophase progression and homologous chromosome pairing. Mol. Biol. Cell 18, 4911–4920. https://doi.org/10.1091/mbc.e07-03-0243.

Jin, J., Cardozo, T., Lovering, R.C., Elledge, S.J., Pagano, M., and Harper, J.W. (2004). Systematic analysis and nomenclature of mammalian F-box proteins. Genes Dev. 18, 2573–2580. https://doi.org/10.1101/gad.1255304.

Jordan, P.W., Karppinen, J., and Handel, M.A. (2012). Polo-like kinase is required for synaptonemal complex disassembly and phosphorylation in mouse spermatocytes. J. Cell Sci. 125, 5061–5072. https://doi.org/10.1242/jcs.105015.

Keeney, S., Lange, J., and Mohibullah, N. (2014). Self-organization of meiotic recombination initiation: general principles and molecular pathways. Annu. Rev. Genet. 48, 187–214. https://doi.org/10.1146/annurev-genet-120213-092304.

Kikuchi, M., Nishimura, T., Ishishita, S., Matsuda, Y., and Tanaka, M. (2020). foxl3, a sexual switch in germ cells, initiates two independent molecular pathways for commitment to oogenesis in medaka. Proc. Natl. Acad. Sci. U S A 117, 12174–12181. https://doi.org/10.1073/pnas.1918556117.

Kipreos, E.T., and Pagano, M. (2000). The F-box protein family. Genome Biol. 1. REVIEWS3002. https://doi.org/10.1186/gb-2000-1-5-reviews3002.

Kojima, M.L., de Rooij, D.G., and Page, D.C. (2019). Amplification of a broad transcriptional program by a common factor triggers the meiotic cell cycle in mice. Elife 8. https://doi.org/10.7554/eLife.43738.

Mahadevaiah, S.K., Turner, J.M., Baudat, F., Rogakou, E.P., de Boer, P., Blanco-Rodriguez, J., Jasin, M., Keeney, S., Bonner, W.M., and Burgoyne, P.S. (2001). Recombinational DNA double-strand breaks in mice precede synapsis. Nat. Genet. 27, 271–276. https://doi.org/10.1038/85830.

Mohammad, A., Vanden Broek, K., Wang, C., Daryabeigi, A., Jantsch, V., Hansen, D., and Schedl, T. (2018). Initiation of meiotic development is controlled by three post-transcriptional pathways in Caenorhabditis elegans. Genetics 209, 1197–1224. https://doi.org/10.1534/genetics.118.300985.

Parra, M.T., Gomez, R., Viera, A., Llano, E., Pendas, A.M., Rufas, J.S., and Suja, J.A. (2009). Sequential assembly of centromeric proteins in male mouse meiosis. PLoS Genet. 5, e1000417. https://doi.org/10.1371/journal.pgen.1000417.

Parra, M.T., Viera, A., Gomez, R., Page, J., Carmena, M., Earnshaw, W.C., Rufas, J.S., and Suja, J.A. (2003). Dynamic relocalization of the chromosomal passenger complex proteins inner centromere protein (INCENP) and aurora-B kinase during male mouse meiosis. J. Cell Sci. 116, 961–974. https://doi.org/10.1242/jcs.00330.

Peters, A.H., Plug, A.W., van Vugt, M.J., and de Boer, P. (1997). A drying-down technique for the spreading of mammalian meiocytes from the male and female germline. Chromosome Res. 5, 66–68.

Qiao, H., Chen, J.K., Reynolds, A., Hoog, C., Paddy, M., and Hunter, N. (2012). Interplay between synaptonemal complex, homologous recombination, and centromeres during mammalian meiosis. PLoS Genet. 8, e1002790. https://doi.org/10.1371/journal.pgen.1002790.

Qiu, X., Hill, A., Packer, J., Lin, D., Ma, Y.A., and Trapnell, C. (2017). Single-cell mRNA quantification and differential analysis with Census. Nat. Methods 14, 309–315. https://doi.org/10.1038/nmeth.4150.

Reitsma, J.M., Liu, X., Reichermeier, K.M., Moradian, A., Sweredoski, M.J., Hess, S., and Deshaies, R.J. (2017). Composition and regulation of the cellular repertoire of SCF ubiquitin ligases. Cell 171, 1326–1339.e14. https://doi.org/10.1016/j.cell.2017.10.016.

Royo, H., Prosser, H., Ruzankina, Y., Mahadevaiah, S.K., Cloutier, J.M., Baumann, M., Fukuda, T., Hoog, C., Toth, A., de Rooij, D.G., et al. (2013). ATR acts stage specifically to regulate multiple aspects of mammalian meiotic silencing. Genes Dev. 27, 1484–1494. https://doi.org/10.1101/gad.219477.113.

Scully, R., Chen, J., Plug, A., Xiao, Y., Weaver, D., Feunteun, J., Ashley, T., and Livingston, D.M. (1997). Association of BRCA1 with Rad51 in mitotic and meiotic cells. Cell 88, 265–275. https://doi.org/10.1016/s0092-8674(00)81847-4.

Shibuya, H., Ishiguro, K., and Watanabe, Y. (2014). The TRF1-binding protein TERB1 promotes chromosome movement and telomere rigidity in meiosis. Nat. Cell Biol. 16, 145–156. https://doi.org/10.1038/ncb2896.

Shimada, R., Koike, H., Hirano, T., Kato, Y., and Saga, Y. (2021). NANOS2 suppresses the cell cycle by repressing mTORC1 activators in embryonic male germ cells. iScience 24, 102890. https://doi.org/10.1016/j.isci.2021.102890.

Shin, Y.H., Choi, Y., Erdin, S.U., Yatsenko, S.A., Kloc, M., Yang, F., Wang, P.J., Meistrich, M.L., and Rajkovic, A. (2010). Hormad1 mutation disrupts synaptonemal complex formation, recombination, and chromosome segregation in mammalian meiosis. PLoS Genet. 6, e1001190. https://doi.org/10.1371/journal.pgen.1001190.

Shinohara, A., and Shinohara, M. (2004). Roles of recA homologues Rad51 and Dmc1 during meiotic recombination. Cytogenet. Genome Res. 107, 201–207. https://doi.org/10.1159/000080598.

Stuart, T., Butler, A., Hoffman, P., Hafemeister, C., Papalexi, E., Mauck, W.M., 3rd, Hao, Y., Stoeckius, M., Smibert, P., and Satija, R. (2019). Comprehensive integration of single-cell data. Cell 177, 1888–1902.e21. https://doi.org/10.1016/j.cell.2019.05.031.

Takemoto, K., Tani, N., Takada-Horisawa, Y., Fujimura, S., Tanno, N., Yamane, M., Okamura, K., Sugimoto, M., Araki, K., and Ishiguro, K.-I. (2020). Meiosis-specific C19orf57/4930432K21Rik/BRME1 modulates localization of RAD51 and DMC1 to DSBs in mouse meiotic recombination. Cell Rep. 31, 107686. https://doi.org/10.1016/j.celrep.2020.107686.

Thorvaldsdóttir, H., Robinson, J.T., and Mesirov, J.P. (2013). Integrative Genomics Viewer (IGV): high-performance genomics data visualization and exploration. Brief. Bioinform. 14, 178–192. https://doi.org/10.1093/bib/bbs017.

Turner, J.M., Aprelikova, O., Xu, X., Wang, R., Kim, S., Chandramouli, G.V., Barrett, J.C., Burgoyne, P.S., and Deng, C.X. (2004). BRCA1, histone H2AX phosphorylation, and male meiotic sex chromosome inactivation. Curr. Biol. 14, 2135–2142. https://doi.org/10.1016/j.cub.2004.11.032.

Wiltshire, T., Park, C., Caldwell, K.A., and Handel, M.A. (1995). Induced premature G2/M-phase transition in pachytene spermatocytes includes events unique to meiosis. Dev. Biol. 169, 557–567. https://doi.org/10.1006/dbio.1995.1169.

Wojtasz, L., Daniel, K., Roig, I., Bolcun-Filas, E., Xu, H., Boonsanay, V., Eckmann, C.R., Cooke, H.J., Jasin, M., Keeney, S., et al. (2009). Mouse HORMAD1 and HORMAD2, two conserved meiotic chromosomal proteins, are depleted from synapsed chromosome axes with the help of TRIP13 AAA-ATPase. PLoS Genet. 5, e1000702. https://doi.org/10.1371/journal.pgen.1000702.

Zhang, F., Tang, D., Shen, Y., Xue, Z., Shi, W., Ren, L., Du, G., Li, Y., and Cheng, Z. (2017). The F-box protein ZYGO1 mediates bouquet formation to promote homologous pairing, synapsis, and recombination in rice meiosis. Plant Cell 29, 2597–2609. https://doi.org/10.1105/tpc.17.00287.

Zhu, Z., Bani Ismail, M., Shinohara, M., and Shinohara, A. (2021). SCF(Cdc4) ubiquitin ligase regulates synaptonemal complex formation during meiosis. Life Sci. Alliance 4. https://doi.org/10.26508/lsa.202000933.

Zickler, D., and Kleckner, N. (2015). Recombination, pairing, and synapsis of homologs during meiosis. Cold Spring Harb. Perspect. Biol. 7. https://doi.org/10.1101/cshperspect.a016626.

iScience
Article

STAR★METHODS

KEY RESOURCES TABLE

REAGENT or RESOURCE	SOURCE	IDENTIFIER
Antibodies		
Mouse anti-FLAG M2 (IB, 1:1000)	Sigma-Aldrich	Cat# F1804 RRID: AB_262044
Rabbit anti-HA (WB, IF, 1:1000)	Abcam	Cat# ab9110 RRID:AB_307019
Rabbit anti-Actin (IF, 1:1000)	Sigma-Aldrich	Cat# A2066 RRID: AB_476693
Mouse anti-MLH1 (IF, 1:500)	BD Biosciences:	Cat# 551092 RRID:AB_394041
Rabbit anti-H3S10P (IF, 1:2000)	Abcam	Cat# ab5176 RRID:AB_304763
Rabbit anti-Histone H3 (IF, 1:1000)	Abcam	Cat# ab1791 RRID: AB_302613
Rabbit anti-SYCP1 (IF, 1:1000)	Abcam	Cat# ab15090 RRID:AB_301636
Mouse anti-γH2AX (IF, 1:1000)	Abcam	Cat# ab26350 RRID:AB_470861
Rabbit anti-RAD51 (IF, 1:500)	Santa Cruz	Cat# SC-8349 RRID:AB_2253533
Rrabbit anti-MSH4 (IF, 1:500)	Santa Cruz	Cat# ab58666 RRID:AB_881394
Rabbit anti-SKP1 (IB, 1:1000)	Abcam	Cat# ab10546 RRID: AB_297285
Rabbit anti-TRF2 (IB, 1:1000)	Novus Biologicals	Cat# NB110-57130 RRID: AB_844199
Rabbit anti-Lamin B (IF, 1:1000)	Santa Cruz	Cat# SC-6216 RRID: AB_648156
Mouse anti-TRF1 (IF, 1:1000)	Shibuya et al., 2014	N/A
Rabbit anti-TRF1 (IB, 1:1000)	Shibuya et al., 2014	N/A
Guinea pig anti-SYCP3 (IF, 1:2000)	Ishiguro et al., 2020	N/A
Rat anti-SYCP3 (IF, 1:1000)	Ishiguro et al., 2020	N/A
Mouse anti-SYCP1 (IF, 1:1000)	Ishiguro et al., 2011	N/A
Rabbit anti-FBXO47 M (WB, 1:1000)	This paper	N/A
Rabbit anti-FBXO47 C (WB, 1:1000)	This paper	N/A
Guinea pig anti-FBXO47 C (WB, 1:1000)	This paper	N/A
Guinea pig anti-H1t (IF, 1:2000)	provided by Marry Ann Handel	N/A
Rabbit anti-BRCA1 (IB, 1:500)	provided by Satoshi Namekawa	N/A
Mouse anti-HA 5D8 monoclonal antibody-coupled Magnet agarose	MBL	Cat# M132-10 RRID:AB_11142502
anti-FLAG M2 monoclonal antibody agarose affinity gel (IP, 50µl per IP of testes extract)	Sigma-Aldrich	Cat# M8823 RRID:AB_2637089
Rabbit anti-HORMAD1	ProteinTech	Cat# 13917-1-AP RRID:AB_2120844
Bacterial and virus strains		
E. coli strain BL21-CodonPlus(DE3)-RIPL	Agilent	Cat# 230280

(Continued on next page)

Continued

REAGENT or RESOURCE	SOURCE	IDENTIFIER
Chemicals, peptides, and recombinant proteins		
Ni-NTA agarose	QIAGEN	Cat# 30210
Tissue-Tek O.C.T. compound	Sakura Finetek	Cat# 4583
Vectashield mounting medium containing DAPI	Vector Laboratory	Cat# H-1200
Superscript III Reverse Transcriptase	Thermo Fisher Scientific	Cat# 18080044
TRIzol reagent	Thermo Fisher Scientific	Cat# 15596018
Ex-Taq polymerase	Takara	Cat# RR001B
ECL prime	GE healthcare	Cat# RPN2232
NuPAGE 4-12 %Bis-Tris Protein Gel	Thermo-Fisher Scientific	Cat# NP0322
CNBr-activated Sepharose	GE healthcare	Cat# 17043001
Pronase	MERCK	Cat# 10165921001
M16 medium	Sigma-Aldrich	Cat# MR016
M2 medium	Sigma-Aldrich	Cat# MR015
3xFLAG peptide	Sigma-Aldrich	Cat# F4799
SimplyBlue	Thermo-Fisher	Cat# LC6065
Pierce DTT, No-Weight Format (48x7.7mg)	Thermo Fisher Scientific	Cat# 20291
Pierce Iodoacetamide, Single-Use (24x9.3mg)	Thermo Fisher Scientific	Cat# 90034
Trypsin/Lys-C Mix, Mass Spec Grad (5x20μg)	Promega	Cat# V5073
cOmplete, EDTA-free	Roche	Cat# 4 693 132
RIPA buffer	Thermo	Cat# 89900
collagenase	Sigma-Aldrich	Cat# C0130
DNase II	Sigma-Aldrich	Cat# 8764
Proteinase inhibitor cocktail	Sigma-Aldrich	Cat# P8340
H&E Staining System	Leica	Cat# 3801698
Cas9 protein	NIPPON GENE	Cat# 317-08441
Glycogen	Wako	Cat# 077-05311
Triton X-100	Sigma-Aldrich	Cat# T9284
PNA lectin	Sigma-Aldrich	Cat# L7381
Opti-MEM I Reduced Serum Medium	Thermo Fisher Scientific	Cat# 31985062
RNasin® Plus Ribonuclease Inhibitors	Promega	Cat# N2611
Giemza	Wako	Cat# 079-04391
Critical Commercial Assays		
MEBSTAIN Apoptosis TUNEL Kit Direct	MBL	Cat# 8445
TB Green Premix Ex Taq II (Tli RNaseH Plus)	Takara	Cat# RR820A
Deposited data		
ChIP-seq data of MEIOSIN and STRA8 data (DDBJ Sequence Read Archive)	Ishiguro et al. 2020	DRA007066, DRA007778, DRA009056
scRNA-seq data of fetal ovaries	Shimada et al. 2021	DRA 011172
Original data	Mendeley Data	https://doi.org/10.17632/ct84bbswv5.2
Experimental models: Organisms/strains		
Mouse: *Fbxo47* knockout	This paper	CARD ID 2777
Mouse: *Fbxo47-3xFLAG-HA* knock-in	This paper	CARD ID 2972
Mouse: *Skp1-3xFLAG-HA* knock-in	This paper	CARD ID 2638
Mouse: C57BL/6N	SLC	N/A

Continued

REAGENT or RESOURCE	SOURCE	IDENTIFIER
Oligonucleotides		
tracrRNA	FASMAC	GE-002
Primers for RT-PCR, genotyping, genome editing	See Table S1	N/A
Recombinant DNA		
pET28c-*Fbxo47*-C (aa272-451)	This paper	RDB19263
pET19b-*Fbxo47*-M (aa174-316)	This paper	RDB19264
Software and algorithms		
genome browser IGV	Thorvaldsdottir et al., 2013	http://meme-suite.org/tools/meme-chip
SoftWorx	GE Healthcare	N/A
CellSens	OLYMPUS	N/A
BZ-X	KEYENCE	N/A
Proteome Discoverer version 1.4	Thermo Fisher Scientific	N/A
Mascot search engine version 2.5	Matrix Science	N/A
Xcalibur	Thermo Fisher Scientific	N/A
Thermal Cycler Dice Real Time System Software	Takara	Ver.5.11B for TP850
Prism8	Graphpad	RRID:SCR_002798

RESOURCE AVAILABILITY

Lead contact

Further information and requests for the resources and reagents should be directed to and will be fulfilled by the Lead Contact, Kei-ichiro Ishiguro (ishiguro@kumamoto-u.ac.jp).

Materials availability

The ChIP-seq data of MEIOSIN and STRA8 are described in our previous study (Ishiguro et al., 2020) and available in the DDBJ Sequence Read Archive (DRA) under accession number DRA007066, DRA007778, DRA009056. Mouse lines generated in this study have been deposited to Center for Animal Resources and Development (CARD), *Fbxo47* Ex3-11Δ knockout mouse (ID 2777), *Fbxo47-3xFLAG-HA* knock-in mouse (ID 2972), and *Skp1-3xFLAG-HA* knock-in mouse (ID 2638). Plasmid expression vectors generated in this study have been deposited to RIKEN BRC: pET28c-*Fbxo47*-C (aa272-451) (ID RDB192639) and pET28c-*Fbxo47*-M (aa174 -316) (ID RDB19264). The antibodies are available upon request. There are restrictions to the availability of antibodies due to the lack of an external centralized repository for their distribution and our need to maintain the stock. We are glad to share antibodies with reasonable compensation by the requestor for its processing and shipping. All unique/stable reagents generated in this study are available from the Lead Contact with a completed Materials Transfer Agreement.

Data and code availability

All data supporting the conclusions are present in the paper and the supplementary materials. The source data (for Figures 1B, 1F, 4C, 4G, 4I, 4J, 5A, 5C, 5F, 5G, 6C–6E, and S3D) are provided in Data S2. The original images for all of the figures in this paper are deposited in public depository Mendeley Data, V1, https://doi.org/10.17632/ct84bbswv5.2. The ChIP-seq data of MEIOSIN and STRA8 (Ishiguro et al., 2020) have been deposited in the DDBJ Sequence Read Archive (DRA) and available under accession number DRA007066, DRA007778, DRA009056. There is no code used in this study.

EXPERIMENTAL MODEL AND SUBJECT DETAILS

Animals

Fbxo47 Ex3-11Δ knockout and *Fbxo47-3xFLAG-HA* knock-in mice were C57BL/6 background (age: 13–21 days old, 8-weeks old). *Skp1-3xFLAG-HA* knock-in mouse was congenic with C57BL/6 background (age: 14–21 days old). Male mice were used for immunoprecipitation of testis extracts, histological analysis of testes, immunostaining of testes, and RT-PCR experiments. Female mice were used for histological

analysis of the ovaries, and immunostaining experiments (age: 8-weeks old). Whenever possible, each knockout animal was compared to littermates or age-matched non-littermates from the same colony, unless otherwise described. Animal experiments were approved by the Institutional Animal Care and Use Committee (approval F28–078, A30–001, A28–026, A2020-006).

METHOD DETAILS

Generation of *Fbxo47* knockout mice and genotyping

Fbxo47 knockout mouse was generated by introducing Cas9 protein (317–08441; NIPPON GENE, Toyama, Japan), tracrRNA (GE-002; FASMAC, Kanagawa, Japan), synthetic crRNA (FASMAC), and ssODN into C57BL/6N fertilized eggs using electroporation. For generating *Fbxo47* Exon3-11 deletion (Ex3-11Δ) allele, the synthetic crRNAs were designed to direct TACACCTAGTGATAGCACTT(GGG) of the *Fbxo47* intron 2 and AGAGCACTAGTCACTGAATG(CGG) in the 3'-neighboring region of the Exon11. ssODN: 5'-GCTCAAAGTAAGCAAAGCAACAGAGAGCACTAGTCACTGATTATTTATTCACTTGGGATGCTGAGGAGGCAAATTGCCAGGTGTTTGAAGC-3' was used as a homologous recombination template.

The electroporation solutions contained (10 μM of tracrRNA, 10 μM of synthetic crRNA, 0.1 μg/μL of Cas9 protein, 1 μg/μL of ssODN) for *Fbxo47* knockout in Opti-MEM I Reduced Serum Medium (31985062; Thermo Fisher Scientific). Electroporation was carried out using the Super Electroporator NEPA 21 (NEPA GENE, Chiba, Japan) on Glass Microslides with round wire electrodes, 1.0 mm gap (45–0104; BTX, Holliston, MA). Four steps of square pulses were applied (1, three times of 3 mS poring pulses with 97 mS intervals at 30 V; 2, three times of 3 mS polarity-changed poring pulses with 97 mS intervals at 30 V; 3, five times of 50 mS transfer pulses with 50 mS intervals at 4 V with 40% decay of voltage per each pulse; 4, five times of 50 mS polarity-changed transfer pulses with 50 mS intervals at 4 V with 40% decay of voltage per each pulse).

The targeted *Fbxo47* Ex3-11Δ allele in F0 mice were identified by PCR using the following primers:

Fbxo47-F1: 5'-TCCTCTCTCTGTCTCTTTATTCAACAG-3' and Fbxo47-R1: 5'- TGCTAAGAAGGTGGTAAAGAATGTGAC-3' for the knockout allele (825 bp). Fbxo47-F3: 5'- TCTGACCATGAACGCTATCTCTTCC-3' and Fbxo47-R1 for wild-type allele (503 bp).

The PCR amplicons were verified by sequencing. Primer sequences are listed in Table S1.

Generation of *Fbxo47-3xFLAG-HA* knock-in mice and genotyping

Fbxo47-3xFLAG-HA knock-in mouse was generated by introducing Cas9 protein, tracrRNA, synthetic crRNA, and ssODN into C57BL/6N fertilized eggs using electroporation as described above. The synthetic crRNA was designed to direct ACGCTATCTCTTCCTAAGTC(AGG) of the *Fbxo47*. ssODN: 5'-GAACTTCCATAAGGAGGTGCTGTATCTGACCATGAACGCTATCTCTTCCGGGAGACTACAAAGACCATGACGGTGATTATAAAGATCATGACATCGATTACAAGGATGACGATGACAAGGGATACCCCTACGACGTGCCCGACTACGCCTAAGTCAGGAAGCTTGTGTCCCTCTGGACTGGCATTCAGGGGAGTGATGCC-3' was used as a homologous recombination template. The targeted *Fbxo47-3xFLAG-HA* knock-in allele in F0 mice were identified by PCR using the following primers:

Fbxo47-F4: 5'-TCTGTTCCATCTTCTCCATGCTCAGGC-3' and Fbxo47-R3: 5'- TGAAGAGCCAGAACTTGTTTTCCAG-3' for the knock-in allele (396 bp), and for wild-type allele (294 bp). The PCR amplicons were verified by sequencing. Primer sequences are listed in Table S1.

Generation of *Skp1-3xFLAG-HA* knock-in mouse and genotyping

The targeting vector was designed to insert 3xFLAG-HA-3'UTR in frame with the coding sequence into the Exon 6 of the *Skp1* genomic locus. Targeting arms of 1225bp and 1481bp fragments, 5' and 3' of the Exon 6 of *Skp1* gene respectively, were generated by PCR from mouse C57BL/6 genomic DNA and directionally cloned flanking p*GK-Neo*-polyA and *DT-A* cassettes. The 5' arm was followed by nucleotide sequences encoding 3xFLAG, HA and the 3'UTR of *Skp1* gene. TT2 ES cells were co-transfected with the targeting vector and pX330 plasmids (Addgene) expressing Crispr-gRNAs directing GCTGGCATTGACTCGGGGTA(ggg) and CGCCACCATACCCGGTGATT (tgg), which locate at the 3' region of the Exon 6 of *Skp1* gene. The G418-resistant ES clones were screened for homologous recombination with the *Skp1* locus by PCR using

primers SKP1_5Arm_F2: 5'- GGTCAGCAACACTGCTGAACAGCTTG-3' and KI96ES-19814R-HA: 5'-GGGCACGTCGTAGGGGTATCCCTTG -3' for the left arm (1909 bp); pKO2-3armF: 5'-AGGAACTTCGGA ATAGGAAC-3' and SKP1_RightArm_R2: 5'-TGCAGTGGAGGCTCAGTCCAGCTTC-3' for the right arm (1897 bp).

The homologous recombinant cells were isolated and chimeric mice were generated by aggregation (host ICR) of recombinant ES cells. Chimeric males were mated to C57BL/6N females and the progenies were genotyped by PCR using the primers:

SKP1onL2_F2: 5'- ATCATTGTTCCCAGGTGGAG -3' and SKP1onRight_R1: 5'- GACTAGAACAAGATGACAGG -3' for the knock-in allele (2078 bp) and the WT allele (1275bp). Primer sequences are listed in Table S1.

Histological analysis

Testes, caudal epididymis and ovaries were fixed in Bouin's solution, and embedded in paraffin. Sections were prepared on CREST-coated slides (Matsunami) at 6 μm thickness. The slides were deparaffinized and stained with hematoxylin and eosin.

For Immunofluorescence staining, testes were embedded in Tissue-Tek O.C.T. compound (Sakura Finetek) and frozen. Cryosections were prepared on the CREST-coated slides (Matsunami) at 8 μm thickness, and then air-dried. The serial sections of frozen testes were fixed in 4% paraformaldehyde in PBS for 5 min at room temperature and washed briefly in PBS. After washing, the serial sections were permeabilized in 0.1% TritonX100 in PBS for 5 min. The sections were blocked in 3% BSA/PBS, and incubated at room temperature with the primary antibodies in a blocking solution. After three washes in PBS, the sections were incubated for 1 h at room temperature with Alexa-dye-conjugated secondary antibodies (1:1000; Invitrogen) in a blocking solution. PNA lectin staining was done using FITC-conjugated Lectin from *Arachis hypogaea* (IF, 1:1000, Sigma: L7381). TUNEL assay was performed using MEBSTAIN Apoptosis TUNEL Kit Direct (MBL 8445). DNA was counterstained with Vectashield mounting medium containing DAPI (Vector Laboratory).

Immunostaining of spermatocytes

Surface-spread nuclei from spermatocytes were prepared by the dry down method as described (Peters et al., 1997) (Takemoto et al., 2020) with modification. The slides were then air-dried and washed with water containing 0.1% TritonX100 or frozen for longer storage at −30ºC. The slides were permeabilized in 0.1% TritonX100 in PBS for 5 min, blocked in 3% BSA/PBS, and incubated at room temperature with the primary antibodies in 3% BSA/PBS. After three washes in PBS, the sections were incubated for 1 h at room temperature with Alexa-dye-conjugated secondary antibodies (1:1000; Invitrogen) in a blocking solution. For bouquet counting, cells were suspended in PBS without hypotonic treatment and structurally preserved nuclei of spermatocytes were prepared by cytospin at 1000 rpm for 5 min (Thermofisher). Cells were fixed with 4% PFA in PBS for 5 min. The slide grasses were washed with PBS containing 0.1% TritonX100 in PBS. After washing with PBS, immunofluorescence staing was perfomed immediately. DNA was counterstained with Vectashield mounting medium containing DAPI (Vector Laboratory).

Imaging

Immunostaining images were captured with DeltaVision (GE Healthcare). The projection of the images was processed with the SoftWorx software program version 7.2.1 (GE Healthcare). All images shown were Z-stacked. Bright field images and immunofluorescent images for counting seminiferous tubules, were captured with BIOREVO BZ-X710 (KEYENCE), and processed with BZ-H3A program. XY-stitching capture by 10x objective lens was performed for multiple-point color images using BZ-X Wide Image Viewer. Images were merged over the field using BZ-H3A Analyzer (KEYENCE). If the SYCP3 image was too dim for counting the SYCP3+ seminiferous tubules, the contrast of the color channel used for SYCP3 was enhanced in the XY-stitched image.

In vitro oocyte culture and Giemsa staining of metaphase chromosome spread

Ovaries collected from 4-week-old female mice were used after 46 to 48 h of treatment with 5 IU of pregnant mare serum gonadotropin. GV oocytes were isolated by puncturing the follicles in M2 medium (Sigma MR-015). The GV oocytes were cultured in M16 medium (Sigma MR-016) in a 5% CO_2 atmosphere

at 37°C for 6h. For Giemsa staining of metaphase chromosome spread, oocytes were exposed to 0.5% Pronase (MERCK 10165921001) to remove the zona pellucida, and treated in hypotonic buffer containing 1% sodium citrate/0.1% PVA for 15min. The oocytes and oocyte-like cells were placed on the slides, fixed in the Carnoy's Fixative (75% Methanol, 25% Acetic Acid), and stained in 3% Giemsa solution for 30min.

Culture of OA-induced meta I spermatocyte

Culture of OA-induced Meta I spermatocytes were performed as described (Wiltshire et al., 1995). The isolated spermatocytes were cultured in the presence or absence of 5 μM okadaic acid (OA) for 3 h.

Antibodies

The following antibodies were used for immunoblot (IB) and immunofluorescence (IF) studies: mouse anti-FLAG M2 (Sigma-Aldrich F1804), rabbit anti-HA (IB, IF, 1:1000, Abcam: ab9110), rabbit anti-Actin (IB, 1:1000, Sigma-Aldrich A2066), mouse anti-MLH1 (IF, 1:500, BD Biosciences: 551,092), rabbit anti-H3S10p (IF, 1:2000, Abcam ab5176), rabbit anti-Histone H3 (IB, 1:1000, Abcam ab1791), rabbit anti-SYCP1 (IF, 1:1000, Abcam ab15090), mouse anti-gH2AX (IF, 1:1000, Abcam ab26350), rabbit anti-RAD51 (IF, 1:500, Santa Cruz: SC-8349), rabbit anti-MSH4 (IF, 1:500, Abcam ab58666), rabbit anti-SKP1 (IB, 1:1000, Abcam ab10546), rabbit anti-HORMAD1 (IF, 1:1000, ProteinTech 13917-1-AP), goat anti-Lamin B (IF, 1:1000, Santa Cruz: SC-6216), mouse anti-TRF1 (Shibuya et al., 2014) (IF, 1:1000), rabbit anti-TRF1 (Shibuya et al., 2014) (IB, 1:1000), rabbit anti-TRF2 (IB, 1:1000, NB110-57130), mouse anti-SYCP1 (IF, 1:1000) (Ishiguro et al., 2011), rat anti-SYCP3 (Ishiguro et al., 2020) (IF, 1:1000), gunia pig anti-SYCP3 (Ishiguro et al., 2020) (IF, 1:2000), rabbit anti-BRCA1 (IF, 1:500, kindly provided by Satoshi Namekawa), guinea pig anti-H1t (IF, 1:2000, kindly provided by Marry Ann Handel).

Production of antibodies against FBXO47

Polyclonal antibodies against mouse FBXO47 C-terminal (aa272-451) were generated by immunizing rabbits and a guinea pig. FBXO47 middle region (aa174-316) were generated by immunizing a rabbit. His-tagged recombinant proteins of FBXO47 middle region (aa174-316) and C-terminal (aa272-451) were produced by inserting cDNA fragments in-frame with pET19b and pET28c (Novagen) respectively in *E. coli* strain BL21-CodonPlus (DE3)-RIPL (Agilent), solubilized in a denaturing buffer (6 M HCl-Guanidine, 20 mM Tris-HCl pH 7.5) and purified by Ni-NTA (QIAGEN) under denaturing conditions. The antibodies were affinity-purified from the immunized serum with immobilized antigen peptides on CNBr-activated Sepharose (GE healthcare).

PCR with reverse transcription

Total RNA was isolated from tissues and embryonic gonads using TRIzol (Thermo Fisher). cDNA was generated from total RNA using Superscript III (Thermo Fisher) followed by PCR amplification using Ex-Taq polymerase (Takara) and template cDNA.

For RT-qPCR, total RNA was isolated from WT (n = 3) and *Meiosin* KO (n = 3) testes, and cDNA was generated as described previously (Ishiguro et al., 2020). *Fbxo47* cDNA was quantified by ΔCT method using TB Green Premix Ex Taq II (Tli RNaseH Plus) and Thermal cycler Dice (Takara), and normalized by *GAPDH* expression level.

qPCR was performed in duplicates, and the average ddCt value was calculated for each cDNA sample. The expression level of *Fbxo47* was divided by that of *GAPDH* to give the relative expression level of *Fbxo47* to *GAPDH*. Relative expression level of *Fbxo47* to *GAPDH* was normalized to 1 for a given P10 WT sample.

Sequences of primers used for RT-PCR were as follows:

GAPDH-F: 5'-TTCACCACCATGGAGAAGGC-3'

GAPDH-R: 5'-GGCATGGACTGTGGTCATGA-3'

Gapdh_F2: 5'-ACCACAGTCCATGCCATCAC-3'

Gapdh_R2: 5'-TCCACCACCCTGTTGCTGTA-3'

Gapdh_Ex6F: 5'-GGTTGTCTCCTGCGACTTCA-3'

Gapdh_mRNAR: 5'-GCCGTATTCATTGTCATACCAGG-3'

Fbxo47-F 1443F: 5'-GCATAGCAAATGCTTTTGCCTGTG-3'

Fbxo47-R 1605R: 5'-GAGATAGCGTTCATGGTCAGATAC-3'

Primer sequences are listed in Table S1.

Preparation of testis extracts and immunoprecipitation

Testis chromatin-bound and -unbound extracts were prepared as described previously (Ishiguro et al., 2014). Briefly, testicular cells collected in PBS containing 1μM MG132, and suspended in low salt extraction buffer (20 mM Tris-HCl pH 7.5, 100 mM KCl, 0.4 mM EDTA, 0.1% Triton X-X100, 10% glycerol, 1 mM β-mer-captoethanol) supplemented with Complete Protease Inhibitor (Roche). After homogenization, the soluble chromatin-unbound fraction was separated after centrifugation at 100,000g for 10 min at 4°C. The chromatin bound fraction was extracted from the insoluble pellet by high salt extraction buffer (20 mM HEPES-KOH pH 7.0, 400 mM KCl, 5 mM MgCl$_2$, 0.1% Tween 20, 10% glycerol, 1 mM β-mercaptoethanol) supplemented with Complete Protease Inhibitor. The solubilized chromatin fraction was collected after centrifugation at 100,000g for 10 min at 4°C.

Immuno-affinity purification

Immuno-affinity purification was performed with anti-FLAG M2 monoclonal antibody-coupled magnetic beads (Sigma-Aldrich M8823) from the testis chromatin-bound and -unbound fractions of *Fbxo47-3xFLAG-HA* knock-in mice and *Skp1-3xFLAG-HA* knock-in mice (14–21-day-old). For negative control, mock immuno-affinity purification was done from the testis chromatin-bound and -unbound fractions from the age-matched wild type mice. The beads were washed with high salt extraction buffer for chromatin-bound proteins and low salt extraction buffer for chromatin-unbound proteins. The anti-FLAG-bound proteins were eluted by 3xFLAG peptide (Sigma-Aldrich). The second immuno-affinity purification was performed anti-HA 5D8 monoclonal antibody-coupled Magnet agarose (MBL M132-10). The bead-bound proteins were eluted with 40 μl of elution buffer (100 mM Glycine-HCl pH 2.5, 150 mM NaCl), and then neutralized with 4 μl of 1 M Tris-HCl pH 8.0.

The immunoprecipitated proteins were run on 4–12% NuPAGE (Thermo-Fisher) in MOPS-SDS buffer and silver-stained with Silver Quest (Thermo-Fisher), immunoblotted or analyzed by LC-MS/MS. For the immunoblot of whole testes extracts from WT, *Fbxo47* KO, and *Fbxo47-3FH* KI mice, lysates were prepared in RIPA buffer and run on 8% Laemmli SDS-PAGE in Tris-Glycine-SDS buffer. Immunoblot images were developed using ECL prime (GE healthcare) and captured by FUSION Solo (VILBER).

Mass spectrometry

The immunoprecipitated proteins were run on 4–12% NuPAGE (Thermo Fisher) by 1 cm from the well and stained with SimplyBlue (Thermo Fisher) for in-gel digestion. The gel containing proteins was excised, cut into approximately 1mm sized pieces. Proteins in the gel pieces were reduced with DTT (Thermo Fisher), alkylated with iodoacetamide (Thermo Fisher), and digested with trypsin and Lysyl endopepti-dase (Promega) in a buffer containing 40 mM ammonium bicarbonate, pH 8.0, overnight at 37°C. The resultant peptides were analyzed on an Advance UHPLC system (ABRME1ichrom Bioscience) connected to a Q Exactive mass spectrometer (Thermo Fisher) processing the raw mass spectrum using Xcalibur (Thermo Fisher Scientific). The raw LC-MS/MS data was analyzed against the NCBI non-redundant pro-tein/translated nucleotide database restricted to *Mus musculus* using Proteome Discoverer version 1.4 (Thermo Fisher) with the Mascot search engine version 2.5 (Matrix Science). A decoy database comprised of either randomized or reversed sequences in the target database was used for false discovery rate (FDR) estimation, and Percolator algorithm was used to evaluate false positives. Search results were filtered against 1% global FDR for high confidence level. All full lists of LC-MS/MS data are shown in Supplementary Data S1 (Excel file).

ChIP-seq data and public RNA-seq data analysis

MEIOSIN ChIP-seq data described in our previous study (Ishiguro et al., 2020) was analyzed for the *Fbxo47* locus. MEIOSIN binding site was shown along with genomic loci from Ensembl on the genome browser IGV.

Single cell RNA-seq data analysis

The scRNA-seq data of fetal ovaries was derived from DRA 011172 (Shimada et al., 2021). 10× Genomics Drop-seq data of mouse adult testis was derived from GEO: GSE109033 (Hermann et al., 2018). Reanalyses of scRNA-seq data were conducted using the Seurat package for R (v.3.1.3) (Stuart et al., 2019) and pseudotime analayses were conducted using monocle package for R: R (ver. 3.6.2), RStudio (ver.1.2.1335), and monocle (ver. 2.14.0) (Qiu et al., 2017) following developer's tutorial.

QUANTIFICATION AND STATISTICAL ANALYSIS

Statistical analyses, and production of graphs and plots were done using GraphPad Prism8 (version 8.4.3) or Microsoft Excel (version 16.48).

Figure 1B Testis RNA was obtained from P8 WT (3 animals), P10 WT (3 animals), P10 *Meiosin* KO (3 animals). qPCR was performed in duplicates, and the average ddCt value was calculated for each cDNA sample. The expression level of *Fbxo47* was divided by that of *GAPDH* to give the relative expression level of *Fbxo47* to *GAPDH*. Relative expression level of *Fbxo47* to *GAPDH* was normalized to 1 for a given P10 WT sample. Bar graph indicates mean with SD. Statistical significance was determined by one-way ANOVA for all the dataset (p = 0.0221). For pairwise comparison between P10 WT and *Meiosin* KO, statistical significance was determined by t test. *p* < 0.05. See Data S2.

Figure 1F RNA was obtained from WT Embryonic ovaries (E12.5 to E18.5). qPCR was performed in triplicates or quadruplicates, and the average ddCt value was calculated for each cDNA sample. The expression level of *Fbxo47* was divided by that of *GAPDH* to give the relative expression level of *Fbxo47* to *GAPDH*. Relative expression level of *Fbxo47* to *GAPDH* was normalized to 1 for a given E12.5 WT sample. Bar graph indicates mean with SD. See Data S2.

Figure 3A Testis sections (P15) were obtained from non-tagged control (3 animals) and *Fbxo47-3FH* KI (3 animals). Number of seminiferous tubules that have HA+/ SYCP3+ cells was counted per the seminiferous tubules that have SYCP3+ spermatocyte cells (84, 85, 45 tubules for non-tagged control, 123, 90, 79 tubules for *Fbxo47-3FH* KI).

Figure 3D Testis sections (P18) were obtained from non-tagged control (3 animals) and *Fbxo47-3FH* KI (3 animals). Number of seminiferous tubules that have HA+/H1t + cells was counted per the seminiferous tubules that have H1t + spermatocyte cells (52, 36, 18 tubules for non-tagged control; 15, 51, 36 tubules for *Fbxo47-3FH* KI).

Figure 4C Quantification of testes/body-weight ratio (mg/g) in *Fbxo47*$^{+/-}$ (8w; n = 4) and *Fbxo47* KO (8w; n = 10) mice. n: the number of animals examined for each genotype. Bar graph indicates mean with SD. Statistical significance was determined by t-test. p < 0.0001. See Data S2.

Figure 4J Cumulative number of pups born from *Fbxo47*$^{+/-}$ (n = 4, all 6-week old at the start point of mating) and *Fbxo47* KO (n = 4, all 6-week old at the start point of mating) females was counted for 18 weeks of breeding. See Data S2.

Figure 5A Quantification of the seminiferous tubules that have H1t+/SYCP3+ cells per the seminiferous tubules that have SYCP3+ spermatocyte cells in *Fbxo47* heterozygous (p18: 62, 61, 29 tubules/animal were counted from n = 3 animals; 8w: 135, 143, 45 tubules/animal were counted from n = 3 animals) and *Fbxo47* KO (p18: 105, 59, 141 tubules/animal were counted from n = 3 animals; 8w: 36, 55, 63, 64, 88, 69, 108 tubules/animal were counted from n = 7 animals) testes. n: the number of animals examined for each genotype. Bar graph indicates mean with SD. Statistical significance was determined by unpaired t-test. p = 0.0012 for *Fbxo47* heterozygous versus *Fbxo47* KO at P18. See Data S2.

Figure 5C Spermatocytes in the four developmental stages (leptotene, zygotene, pachytene, and diplotene(-like)) per total cells in meiotic prophase I were quantified in WT (n = 727 from one animal) and *Fbxo47* KO (n = 659 from one animal) at P15, and in WT (n = 561 from one animal) and *Fbxo47* KO (n = 516 from one animal) at P18. See Data S2.

Figure 5F Spermatocytes in the four developmental stages (leptotene or zygotene, pachytene, and diplotene(-like)) per total cells in meiotic prophase I were quantified in *Fbxo47*$^{+/-}$ (n = 105 for OA -, 117 for OA+) and *Fbxo47* KO (n = 140 for OA -, 117 for OA+). See Data S2.

Figure 5G Quantification of the seminiferous tubules that have TUNEL + cells per total tubules in *Fbxo47*$^{+/-}$ (8w: n = 3) and *Fbxo47* KO (8w: n = 3) testes. Bar graph indicates mean with SD. Statistical significance was determined by t-test. p = 0.0072. See Data S2.

Figure 6C Numbers of RAD51 foci on SYCP3 axes were counted in WT and *Fbxo47* KO. Number of foci was indicated in the scatterplot with median. Statistical significance was determined by Mann-Whitney U-test. ****: $p < 0.0001$. ***: $p < 0.001$. **: $p < 0.01$. See Data S2.

Figure 6D Numbers of MSH4 foci on SYCP3 axes were counted in WT and *Fbxo47* KO. Number of foci was indicated in the scatterplot with median. Statistical significance was determined by Mann-Whitney U-test. $p < 0.05$. See Data S2.

Figure 6E Numbers of MLH1 foci on SYCP3 axes were counted in *Fbxo47*$^{+/-}$ pachyene (n = 15), or *Fbxo47* KO pachyene (n = 13) and diplotene-like (n = 13). Number of foci was indicated in the scatterplot with median. Statistical significance was determined by Mann-Whitney U-test. $p < 0.0001$. See Data S2.

Figure S3D The frequency of bouquet stage spermatocytes nuclei in wild-type (n = 355) and *Fbxo47* KO (n = 342) was scored at 12 day post-partum. Statistical significance was determined by Chi square-test. p = 0.5025. See Data S2.